



THE HONG KONG
POLYTECHNIC UNIVERSITY

香港理工大學

Pao Yue-kong Library

包玉剛圖書館

Copyright Undertaking

This thesis is protected by copyright, with all rights reserved.

By reading and using the thesis, the reader understands and agrees to the following terms:

1. The reader will abide by the rules and legal ordinances governing copyright regarding the use of the thesis.
2. The reader will use the thesis for the purpose of research or private study only and not for distribution or further reproduction or any other purpose.
3. The reader agrees to indemnify and hold the University harmless from and against any loss, damage, cost, liability or expenses arising from copyright infringement or unauthorized usage.

IMPORTANT

If you have reasons to believe that any materials in this thesis are deemed not suitable to be distributed in this form, or a copyright owner having difficulty with the material being included in our database, please contact lbsys@polyu.edu.hk providing details. The Library will look into your claim and consider taking remedial action upon receipt of the written requests.

**TUNABLE PLASMONIC DEVICES
IN GOLD/DIELECTRIC NANOSTRUCTURES**

NG KI FUNG

M.Phil.

The Hong Kong Polytechnic University

2015



THE HONG KONG
POLYTECHNIC UNIVERSITY

香港理工大學

Department of Applied Physics

Tunable Plasmonic Devices In Gold/Dielectric Nanostructures

Ng Ki Fung

A thesis submitted in partial fulfillment of the requirements for
the degree of Master of Philosophy

May, 2014

CERTIFICATE OF ORIGINALITY

I hereby declare that this thesis is my own work and that, to the best of my knowledge and belief, it reproduces no material previously published or written, nor material that has been accepted for the award of any other degree or diploma, except where due acknowledgement has been made in the text.

_____ (Signed)

_____ NG KI FUNG (Name of student)



Abstract

This thesis presents the studies on the optical properties and applications of three types of periodic plasmonic structures, which were investigated by simulation using the Rigorous Coupled Wave Analysis (RCWA) method, and by experiments through angular-dependent reflectivity measurements. The optical responses such as reflectivity, transmittance and electric field enhancement at the nanometer scale depend on the shape and size of nanostructures, which play pivotal roles in the design of devices based on the surface plasmon resonance (SPR) effect.

First of all, two-dimensional plasmonic nano-pillar structures were simulated. In such samples with Au/photoresist as the metal/dielectric materials, a thin gold layer was deposited perpendicularly on photoresist pillars, leading to isolated gold caps on dielectric pillars that are in turn surrounded by a perforated gold film. Propagating surface plasmon resonances (PSPRs) on the perforated film, and localized surface plasmon resonances (LSPRs) at the gold caps, were simultaneously observed in such a structure. For the electric field distribution, the incident wave was confined at the Amonil pillars due to the coupling of resonant modes for the perforated gold film and



the isolated gold capping layer. Reflection dips were blue-shifted and became sharper with increasing height of the dielectric pillars. The usage of such a device structure for refractive index sensing was discussed.

For the second part of the project, plasmonic Au nanostructures with fractal behavior were investigated by RCWA technique. Fractal patterns that show self-similar behavior and space-filling geometrical arrangement can cause unique optical properties such as transmission enhancement. A type of fractal nanostructure based on Au film/glass substrate system was investigated in this thesis. The fractal pattern was named as center fractal nanostructure in the thesis, as the self-similarity effect occurs at the center of the structure. The effects of three structural parameters (edge length, periodicity and order) on the SPR (transmission dip) were studied. The electric field intensity enhancement factor was boosted with increasing order of the fractal pattern nanostructure. In particular, an electric-field intensity enhancement of ~ 70 times was achieved for the 3rd order fractal pattern studied in this work. As compared with a continuous planar gold film on glass, transmission enhancement peaks were observed in the fractal nanostructure, and the transmission peak positions were controlled by the edge length of the fractal nanostructure. Properly designed nanostructures are known to produce so-



called hot spots for locally enhancing the incident wave intensity. Such a structure is of potential for center fractal nanostructure to be used in antennas.

Finally, SPR tuning via thermally-induced refractive index change in ferroelectric polymer P(VDF-TrFE) was studied. The transition behavior of the copolymer was found to be dependent on the thermal history. The refractive indices of P(VDF-TrFE) were 1.3886 and 1.3637 at 633 nm and 80°C during heating and cooling processes respectively. One-dimensional gratings with periodicity 750 nm were used to excite the SPR. The resonant wavelength was found to change during the heating and cooling process. The experimental results of reflectivity measurement were compared with the simulation results. The results indicated the feasibility of bistable SPR in solid-state structures.



List of publications

1. K.F. Ng, C.W. Leung and K.L. Jim, 'Influence of center fractal patterns on the transmission spectrum and electric field intensity enhancement in gold/glass plasmonic nanostructures', *Microelectronic Engineering* **119**, 79 (2014).



Acknowledgements

First of all, I would like to express my heartfelt grateful to my supervisors, Dr. C. W. Leung and Dr. K. L. Jim, for their invaluable guidance, support, encouragement and patience throughout the whole period of my research study. Without their enlightenment, this thesis would not have been possible.

I would like to thank Dr. D. H. C. Ong and Mr. Z. Cao from Department of Physics at the Chines University of Hong Kong for their assistance in reflectivity measurements.

My genuine thanks go to Miss. S. M. Ng for her great assistance about nanofabrication, and Dr. J. Z. Xin for her kind assistance and helpful advices in both the theory and experiments of plasmonic nanostructure.

Thanks also go to Dr. T.L. Wong for his great assistance in ICP etching and UV lithography in clean room. I would like to thank my colleagues and friends for their assistance and discussions during my research work. They include (in no particular order): Mr. K. Au, Miss Y. Sun, Mr. W. C. Lo, Mr. T. P. Yip, Mr. W. C. Wong, Miss. S. Y. Choi, Miss H. M. Yau and Mr. K. W. Mak. I would like to thank my family and brothers and sisters in my church for their endless love and support. Last but not least, I would like to express my deepest appreciation to my God.



Table of Contents

| | |
|--|-----|
| Abstract..... | II |
| List of publications | V |
| Acknowledgements..... | VI |
| Table of Contents | VII |
| List of figures..... | XI |
| Chapter 1 Introduction | 1 |
| 1.1 Background | 1 |
| 1.2 Scope of present study | 2 |
| 1.3 Contribution of co-workers | 4 |
| 1.4 Literature review | 4 |
| 1.4.1 Electromagnetic theory of surface plasmons | 4 |
| 1.4.2 Surface plasmon resonance based on periodic structure..... | 8 |
| 1.4.3 Surface plasmon resonance based on fractal plasmonic structure | 8 |
| 1.4.4 Thermal tuning of surface plasmon resonance | 10 |
| 1.4.5 Applications of surface plasmon..... | 13 |
| 1.4.5.1 Solar cell | 13 |
| 1.4.5.2 Chemical and biological sensors..... | 13 |
| 1.5 Summary | 14 |



| | |
|--|----|
| Chapter 2 Methodology | 16 |
| 2.1 Introduction..... | 16 |
| 2.2 Simulation method | 16 |
| 2.2.1 Rigorous Coupled Wave Analysis (RCWA) | 16 |
| 2.3 Fabrication techniques | 19 |
| 2.3.1 Soft ultraviolet nanoimprint patterning..... | 19 |
| 2.3.2 Inductive couplong plasma (ICP) etching..... | 21 |
| 2.3.3 D.C. magnetron sputtering..... | 22 |
| 2.4 Characterization technique..... | 24 |
| 2.4.1 Scanning electron microscope (SEM)..... | 24 |
| 2.4.2 Atomic force microscope (AFM)..... | 24 |
| 2.4.3 Ultraviolet–visible spectroscopy..... | 26 |
| 2.4.4 Angular dependent reflectivity..... | 27 |
| 2.5 Summary | 28 |
| Chapter 3 Optical analysis of periodic plasmonic nano-pillars | 29 |
| 3.1 Introduction..... | 29 |
| 3.2 Fabrication of periodic plasmonic nano-pillars | 31 |
| 3.3 Characterization of periodic plasmonic nano-pillars | 33 |
| 3.3.1 Structural characterization of periodic plasmonic nano-pillars | 33 |
| 3.3.2 Opitcal characterization of periodic plasmonic nano-pillars | 35 |
| 3.4 Theoretical study of periodic plasmonic nano-pillars..... | 36 |
| 3.4.1 Numerical simulation..... | 36 |



| | |
|---|----|
| 3.4.2 Influence of height of periodic plasmonic nano-pillar on reflection spectra and electric field intensity distribution..... | 38 |
| 3.5 Application of periodic plasmonic nano-pillars..... | 48 |
| 3.5.1 Refractive index sensor..... | 49 |
| 3.6 Summary..... | 50 |
| Chapter 4 Analysis of plasmonic Center Fractal pattern..... | 52 |
| 4.1 Introduction..... | 52 |
| 4.2 Theoretical study of plasmonic Center Fractal..... | 54 |
| 4.2.1 Simulation model..... | 54 |
| 4.2.2 Influence on electric intensity distribution with different structural parameters (periodicity and order) and compare with Sierpiński Carpet..... | 57 |
| 4.2.3 Influence on transmission spectra and reflection spectra with different structural parameters and compare with Sierpiński Carpet..... | 63 |
| 4.3 Summary..... | 67 |
| Chapter 5 Thermally tunable plasmonic resonance based on ferroelectric polymer P(VDF-TrFE)..... | 69 |
| 5.1 Introduction..... | 69 |
| 5.2 Fabrication of plasmonic structure based on ferroelectric polymer P(VDF-TrFE)..... | 71 |
| 5.3 Characterization of plasmonic structure based on ferroelectric polymer P(VDF-TrFE)..... | 73 |



THE HONG KONG POLYTECHNIC UNIVERSITY

5.3.1 Optical characterization of ferroelectric polymer P(VDF-TrFE)..... 73

5.3.2 Computational study of surface plasmon resonance of ferroelectric polymer
P(VDF-TrFE) 75

 5.3.2.1 Simulation model 75

 5.3.2.2 Surface plasmon resonance of ferroelectric polymer..... 77

5.4 Summary 80

Chapter 6 Conclusions 81

References 84



List of Figures

- Fig. 1.1 (a) Schematic illustration of electromagnetic wave and surface charge at the interface between dielectric material and metal, (b) the local electric field component is enhanced near the surface and decay exponentially with distance in a direction normal to the interface.
- Fig. 1.2 Dispersion relationship of bulk plasmon and SP at metal-dielectric interface.
- Fig. 1.3 The transmission spectra of Hilbert Curve of different orders
- Fig. 1.4 Nonlinear dielectric permittivities of initially poled 70/30 mol% P(VDF-TrFE) copolymer as function of temperature (heating and cooling cycle).
- Fig. 2.1 (a) A simple simulation structure and definition of terms (different colors represent different materials). (b) The effect of the index resolution on the simulation layer: the leftmost is original structure, the middle is a coarse index resolution and the rightmost is a fine index resolution.
- Fig.2.2 Soft ultraviolet nanoimprint patterning procedures for preparing patterns on nano-imprint resist.
- Fig. 2.3 Schematic diagram (a) and the actual setup (b) of the dc magnetron sputtering system used in this work.
- Fig. 2.4 Schematic of the major components of an AFM.
- Fig. 2.5 Ultraviolet–visible spectroscopy used in this work
- Fig. 2.6 Schematic diagram of the visible range angular-dependent reflection measurement system
- Fig. 3.1 Schematic of the process flow for sample fabrication.
- Fig. 3.2 (a) Top view of the SEM images of periodic plasmonic nano-pillars.
(b) AFM image and sectional profiles of periodic plasmonic nano-pillars.
- Fig. 3.3 (a) Simulated and (b) measured angular dispersion relationships of



THE HONG KONG POLYTECHNIC UNIVERSITY

periodic plasmonic nano-pillars with 70 nm-tall pillars. TM-polarized light was used in the calculations and measurements.

- Fig. 3.4 Schematic of isometric view (a) and cross-sectional view (b) of the simulation model.
- Fig. 3.5 Side view of periodic plasmonic nano-pillars with height less than (a) and larger than (b) the gold layer thickness.
- Fig. 3.6 Simulated reflectivity spectra of periodic plasmonic nano-pillar with different heights ($H = 24\text{nm}$, 26nm and 28nm).
- Fig. 3.7 Electric field intensity distribution of the periodic nano-pillar with $H = 40\text{ nm}$ at the reflection dip of wavelength = 1889 nm , normalized to the maximum field intensity. The maximum field intensity enhancement factor under such a condition is 492.
- Fig. 3.8 Simulated reflection spectra with different heights of nano-pillars from $H = 0$ (continuous gold film) to $H = 100\text{ nm}$. D1 is a LSPR and D2 is a CSPR reflection dip.
- Fig. 3.9 Simulated reflection dips D1 with different heights of periodic nano-pillars.
- Fig. 3.10 Simulated reflection dips D2 with different heights of periodic nano-pillars.
- Fig. 3.11 The electric field intensity distribution at reflection dip (D1) with different heights of nano-pillars. The maximum electric field intensity of incoming wave is normalized to 1.
- Fig. 3.12 The normalized electric field intensity distribution at the reflection dip (D2) with different heights of nano-pillars.
- Fig. 3.13 Reflection dispersion relationship with $H = 50\text{nm}$.
- Fig. 3.14 Normalized electric field intensity distribution at different resonance modes: (a) Au/air (1,0), (b) Au/Amonil(1,0) and (c) CSPR.
- Fig. 3.15 Reflection spectra with different heights of nano-pillars at incident angle = 40° .
- Fig. 3.16 (a) Simulated reflection spectra of the periodic plasmonic nano-pillars with different refractive indices at the angle of 50° and $H = 50\text{ nm}$. (b)



THE HONG KONG POLYTECHNIC UNIVERSITY

- The relationship between resonant wavelength and refractive index at the angle of 50° and $H = 50$ nm.
- Fig.4.1 Schematic of the first three orders of the (a) center fractal pattern and (b) Sierpiński carpet. (c) Schematic of periodic fractal pattern nanostructure. The black regions represent gold and white areas correspond to air.
- Fig 4.2 The intensity enhancement factor with different periodicities at $\lambda_o = 800$ nm.
- Fig. 4.3 (a) The intensity enhancement at the center of the basic unit of center fractal nanostructure with different orders for $l_o = 1 \mu\text{m}$. (b) Electric field intensity distribution of the center fractal structure with $n = 1, 2, 3$ at $\lambda = 800$ nm. (c) Electric field intensity distribution of the Sierpiński carpet with $n = 3$. (d) Electric field distribution of an air square with length $l_o/27$ at the center of the basic unit in the continuous planar gold film. Small figures next to (c) and (d) indicate the geometric structures of the corresponding Sierpiński carpet and single air hole.
- Fig. 4.4 Maximum electric field intensity enhancement factor with different orders of the center fractal.
- Fig. 4.5 (a) Transmission spectra of fractal nanostructures with different edge lengths of basic unit for $n = 3$. (b) Relationship between the resonant wavelengths of the third peak of transmission of fractal nanostructures and different edge lengths of basic unit for $n = 3$. (c) Transmission spectra of different orders with edge length $l_o = 1 \mu\text{m}$ and planer gold without pattern.
- Fig. 5.1 Schematic of process flow for fabrication of Au/P(VDF-TrFE) grating structure.
- Fig. 5.2 AFM image (upper panel) and sectional profile (lower panel) of the grating pattern after nanoimprint lithography. The depth of the grating was about 140nm.
- Fig. 5.3 Temperature dependence of refractive index of P(VDF-TrFE) at 633 nm



THE HONG KONG POLYTECHNIC UNIVERSITY

incident wavelength, as measured by ellipsometry.

- Fig. 5.4 Schematic of the simulation model.
- Fig. 5.5 Simulated reflection spectra of 30, 80 and 130°C in (a) heating and (b) cooling at 20° incident angle.
- Fig. 5.6 Measured reflection spectra of 30 °C and 130°C at 20° incident angle.
- Fig. 5.7 Calculated resonant wavelengths in heating and cooling at 20° incidence angle.



Chapter 1

Introduction

1.1 Background

In the last few decades, there was a rapid development in various optical techniques. However, it is difficult for conventional photonic devices to reduce the element sizes to the nanometer scale due to Abbe's diffraction limit (about one-half of the optical wavelength). Excitation of surface plasmon polaritons (SPPs) can overcome the diffraction limit and offer a promising approach to control and manipulate the propagation and dispersion of light in the nanometer scale [1].

The first scientific study of surface plasmon was reported in 1902, when Wood observed an unexplained optical reflection from metallic gratings [2]. Then, bright color in metal-doped glasses was observed by Maxwell and Garnett [3]. In 1908, Mie developed the theory of light scattering by spherical particles [4]. Pines proposed the characteristic energy losses experienced by fast electrons travelling through metals in 1956, and attributed these losses to collective oscillations of free electrons in the metal, which was called "plasmons" [5]. In the same year, Fano suggested the term "polaritons" for the



coupled oscillation of bound electrons and light inside the transparent media [6]. After a year, Ritchie gave the first theoretical description of surface plasmons [7]. The plasmon modes were found to exist near the surface of metals, and he described the anomalous behavior of metal gratings in term of surface plasmon resonance (SPR) excited on the gratings [8]. Otto and Kretschmann suggested optical excitation of surface plasmons on metal films [9]. After the early days of surface plasmon research, the attention gradually changed to applications of surface plasmons [1]. Various surface plasmon-based optical devices and techniques have been developed, such as waveguides [10-17], solar cells [18-21], chemical sensing [22-24] and biosensing [25-32], etc.

1.2 Scope of the present study

The main objective of this research is to study the optical properties and applications of three types of periodic plasmonic nanostructures, which were studied by simulation using the Rigorous Coupled Wave Analysis (RCWA) method and by experiments. The optical responses such as reflectivity, transmittance, and electric field intensity enhancement at the nanometer scale depend on the shape and size of the nanostructures, which play pivotal roles in the design of devices based on the SPR effect.



This thesis consists of six chapters. After an introduction and literature review about the theory of surface plasmon and recent research in this Chapter, methodologies of the simulation and experiments are given in Chapter 2.

In Chapter 3, two-dimensional plasmonic nano-pillar structures consisting of top gold caps and perforated gold films were studied. The optical response of the nano-pillar structures was studied by simulations and experiments. Propagating surface plasmon resonances (PSPRs) on the perforated films, and localized surface plasmon resonances (LSPRs) at the gold caps, were simultaneously observed in such a structure. Also, the coupling surface plasmon resonances (CSPRs), which were formed by the coupling between two types of SPRs, were observed in the structure.

In Chapter 4, the center fractal nanostructures were designed for boosting the electric field intensity enhancement performance. The fractal pattern shows self-similar behavior and space-filling geometrical arrangement, and can cause some unique optical properties such as transmission enhancement. The effects of different structural parameters (edge length, periodicity and order) on the SPRs were studied.

In Chapter 5, tunable surface plasmon structures working in the visible range was designed and implemented. One-dimensional gratings were constructed from gold and



ferroelectric polymer P(VDF-TrFE) thin films. The shift of SPR position by thermal tuning was observed.

Conclusions are then given in Chapter 6.

1.3 Contribution of co-workers

Dr. C.W. Leung, Dr K. L. Jim and I conceived ideas and designed simulation models and experiments. I performed all the RCWA simulations and the angular reflectivity experiments, with the assistance from collaborators in the Chinese University of Hong Kong. X. Fang measured the refractive of ferroelectric polymer P(VDF-TrFE). I performed the analysis of data.

1.4 Literature review

1.4.1 Electromagnetic theory of surface plasmons

Surface plasmons are quantized electromagnetic surface waves that are localized at the interface between a metal and a dielectric material [33]. Electrons are bounded to the atoms in the case of dielectric materials, or they are free to move around as in the case of metals. The dielectric constant of a material strongly depends on the response of the electrons to the external field. For dielectric materials, the dielectric constant (ϵ_{d1} for the real part and ϵ_{d2} for the imaginary part) can be expressed in terms of the Lorentz



model as [34, 35]:

$$\varepsilon_{d1} = \frac{\omega_p(\omega_o^2 - \omega)}{(\omega_o^2 - \omega) + \gamma^2\omega^2} \quad (1.1)$$

$$\varepsilon_{d2} = \frac{\omega_p^2\gamma\omega}{(\omega_o^2 - \omega) + \gamma^2\omega^2} \quad (1.2)$$

where ω is the frequency of the electric field, ω_o is the natural oscillation frequency describing the restoring force, γ is the damping coefficient describing the energy loss due to scattering, ω_p is the plasma frequency defined as $\omega_p = n_e e^2 / m_e \varepsilon_o$, n_e is the electron density and m_e and e are the mass and charge of an electron, respectively.

In the case of metals, the dielectric constant (ε_{m1} and ε_{m2} for real and imaginary parts) is described by the Drude model as [33-35]:

$$\varepsilon_{m1} = 1 - \frac{\omega_p^2}{\omega^2 + \gamma^2} \quad (1.3)$$

$$\varepsilon_{m2} = \frac{\omega_p^2\gamma}{\omega(\omega^2 + \gamma^2)} \quad (1.4)$$

Upon external excitation, the free electrons in the metal oscillate and form possible electromagnetic (EM) waves. At the plasma frequency ω_p , dielectric constant is zero in both real and imaginary parts. No transverse EM wave exists in the material. The pure longitudinal wave corresponds to a collective oscillation of the electrons in the direction of the wave propagation, which is called plasma oscillation.

By solving the Maxwell's equations for plasmons at the interface of semi-infinite metal



and dielectric, the plasmonic dispersion relation is given by [36]:

$$k_{spp} = \frac{2\pi}{\lambda} \sqrt{\frac{\epsilon_m \epsilon_d}{\epsilon_m + \epsilon_d}} \quad (1.5)$$

where k_{spp} is the wave number of the SPP, λ is the incident wavelength, ϵ_m and ϵ_d are real dielectric constants of the metal and dielectric materials respectively.

The plasmon dispersion relation of a flat metal-dielectric interface is given in Fig. 1.1.

The surface charge and field distribution is shown in Fig. 1.1 (a). Fig. 1.1(b) shows that the local field is enhanced near the interface between dielectric and metal, and decays exponentially with distance in a direction normal to the interface [1]. The dispersion relations of bulk plasmon and SP are shown in Fig. 1.2. The dispersion relation of EM wave in the bulk of metal is :

$$c^2 k^2 = \omega^2 - \omega_p^2 \quad (1.6)$$

The propagating solution for bulk plasmon only exists when $\omega > \omega_p$ and it is always above the light line in the free space ($k < \frac{\omega}{c}$). The plasmon wavelength is always longer than that of the free-space photon. This mode propagates into the bulk and is also called radiative plasmon (RP). The case is defined as surface plasmon when $\epsilon_d + \epsilon_m > 0$.

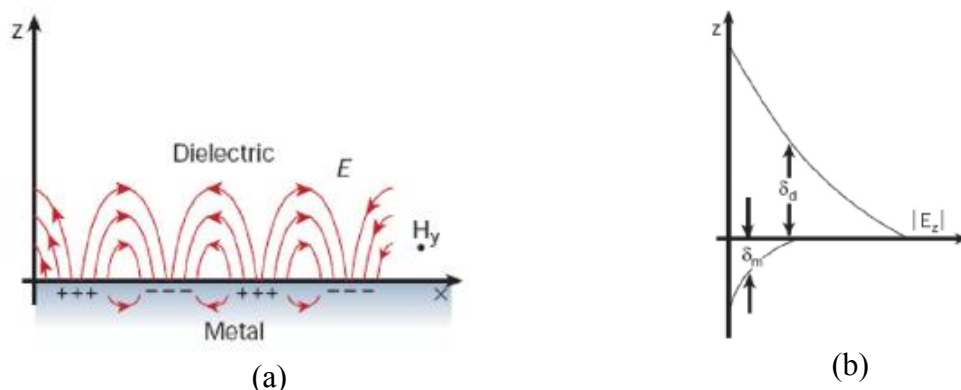


Fig. 1.1 (a) Schematic illustration of electromagnetic wave and surface charge at the interface between dielectric material and metal. (b) The local electric field component is enhanced near the surface and decays exponentially with distance in a direction normal to the interface [1].

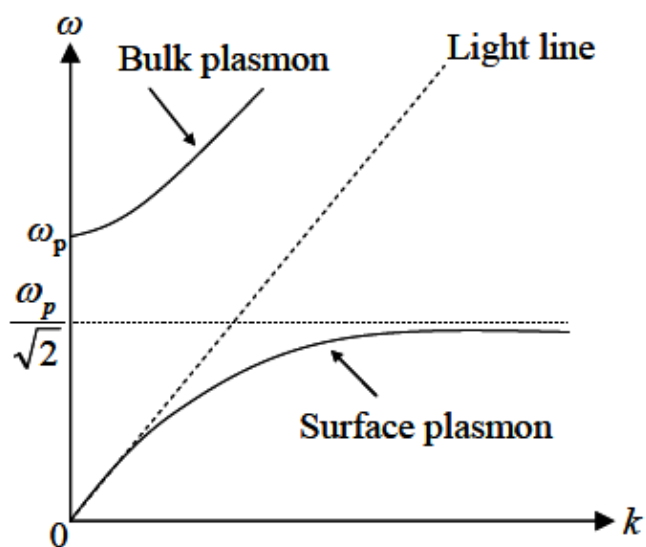


Fig.1.2 Dispersion relationship of bulk plasmon and SP at metal-dielectric interface [37].



1.4.2 Surface plasmon resonance based on periodic structure

In order to excite SPP optically based on the diffraction of light incident on one dimensional (1-D) or two dimensional (2-D) periodic structures, incident wave vector k_{in} couples to one dimensional (1-D) grating vector \mathbf{G} , whose modulus is given by [38]:

$$G = \frac{2\pi}{\Lambda} \quad (1.7)$$

where Λ is the grating period. Each diffraction order holds a vector:

$$k_{in} \sin \theta + nG = \frac{2\pi}{\lambda} \sqrt{\frac{\epsilon_m \epsilon_d}{\epsilon_m + \epsilon_d}} \quad (1.8)$$

where n is the diffraction order, θ is the incident angle and λ is the incident wavelength.

Incident light of k_{in} can also couple to 2-D periodic structures (such as 2-D periodic nanohole arrays) with vector \mathbf{G} , whose modulus is given by [39]:

$$k_{in} \sin \theta + iG_x + jG_y = \frac{2\pi}{\lambda} \sqrt{\frac{\epsilon_m \epsilon_d}{\epsilon_m + \epsilon_d}} \quad (1.9)$$

where i and j are diffraction orders that couple the incident light with a particular mode of the structure.

1.4.3 Surface plasmon resonance based on fractal plasmonic structure

Recently, the concept of fractal geometry was combined with electromagnetic theory to design nanostructures for different optical applications such as antennas, sub-



wavelength imaging, sub-diffraction focusing and so on [40-42].

Fractal is a structure made of patterns which are similar to the whole structure in some way iteratively [43]. The resulting structure may exhibit special properties, such as zero and infinite perimeters at the same time [44]. This concept is used in the design of fractal plasmonic structures, which have self-similar and space-filling geometric arrangements, that can result in some interesting electromagnetic properties [44, 45]. Self-similar properties of the fractals are translated into its electromagnetic behavior [46, 47].

Fractal plasmonic structures have previously been demonstrated. For example, nanoscale fractal apertures allow for enhanced transmission and resolution [41]. Fig. 1.3 shows the transmission spectra of Hilbert Curve structure, which shows an increased transmission efficiency with the order of the structure [48]. Sederberg *et al.* reported a larger perimeter-footprint ratio in higher-order Sierpiński triangle fractal structures as compared with the basis shape, causing a red-shift in the resonance conditions [44]. The resolution of sub-wavelength imaging achieved $\lambda/15$ at infrared range by periodic H-fractal apertures was demonstrated by Huang *et al.* [40]. Vople *et al.* used the Sierpiński carpet structure to control a broadband spectral response, by varying the degree of the

fractal complexity for trapping nano-objects [42].

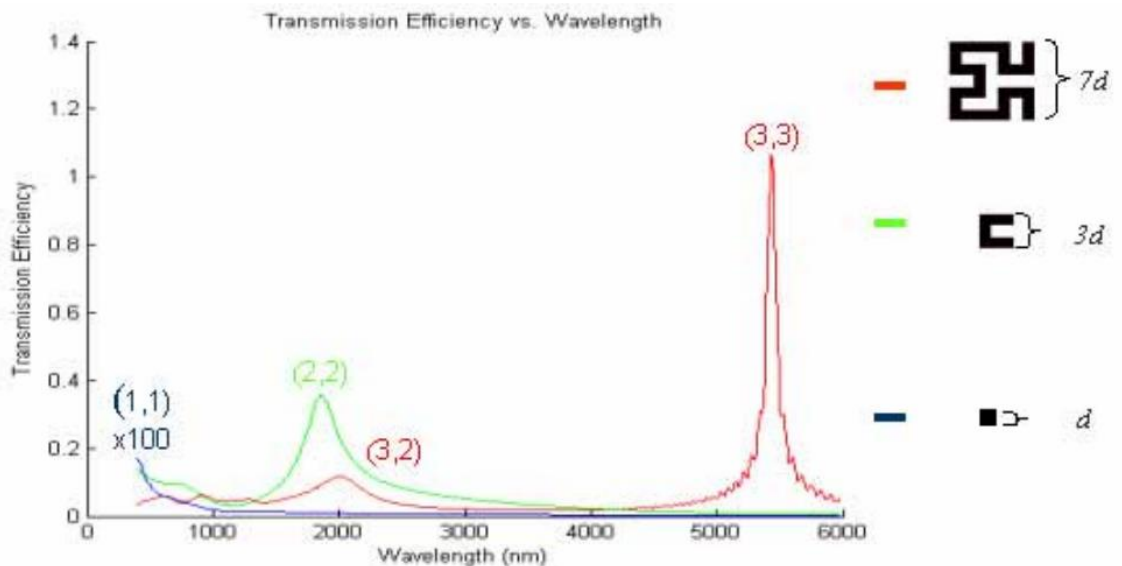


Fig. 1.3 The transmission spectra of Hilbert Curve of different orders [48].

1.4.4 Thermal tuning of surface plasmon resonance

Thermal tuning is one of the approaches for modulating SPRs, with the advantage of simplicity in device fabrication and control of properties. As SPRs is strongly dependent on the dielectric properties of the materials, which in is turn temperature-dependent, heat can be a means of controlling the SPR behavior [1].

Suh *et al.* reported the thermally modulated SPRs in metal nano-particles on the top of



VO₂ film that is common used for thermally tuning SPRs [49, 50]. They also demonstrated the thermally modulated extraordinary transmission in Ag/VO₂ hole arrays prepared by focused ion beam etching [50]. There is a limitation of VO₂ in fabrication, as it is not easy to find a suitable metal mask material whose etchant does not remove with VO₂ that can react with acid solutions [51].

Xin *et al.* reported Ag strips fabricated on flat (Ba,Sr)TiO₃ (BST) for thermally-tunable optical devices. The refractive index increased by 0.002 from room temperature to 66°C [52]. Epitaxial BST thin films grown on single-crystal substrates showed low optical losses and good tunability by electric field and temperature [53-55]. Jim *et al.* reported a band gap shift by 2 nm when a dc voltage of 240V was applied to a 1D photonic crystals based on Ba_{0.7}Sr_{0.3}TiO₃/MgO multilayers [55].

Poly-vinylidene fluoride (PVDF) was the first identified ferroelectric polymer, which shows no Curie temperature as melting occurs prior to the ferroelectric phase transition [56]. The incorporation of trifluoroethylene (TrFE) into PVDF greatly facilitates the formation of the ferroelectric phase [57]. Ploss *et al.* reported a nonlinear dielectric response of P(VDF-TrFE) copolymer with temperature, as evident from the existence of dielectric hysteresis loops (Fig. 1.4) [58].

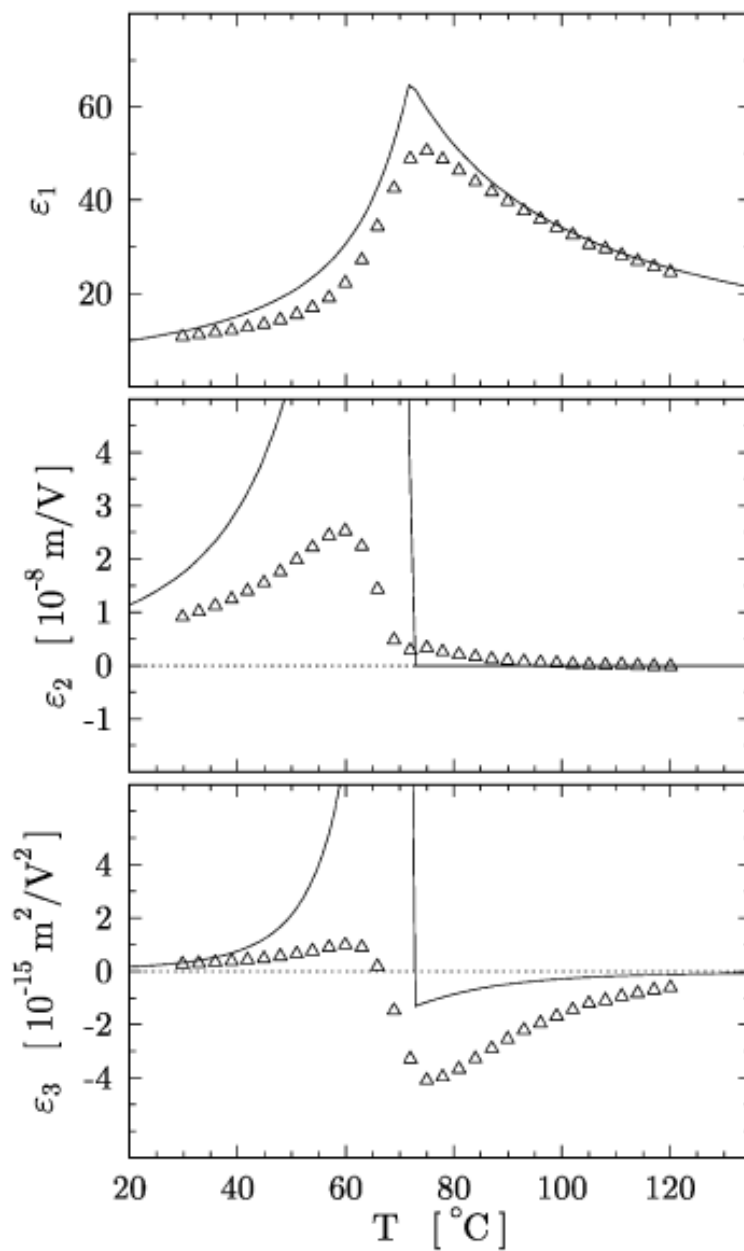


Fig. 1.4 Nonlinear dielectric permittivities of initially poled 70/30 mol% P(VDF-TrFE) copolymer as function of temperature (heating and cooling cycle) [58].



1.4.5 Applications of surface plasmon

1.4.5.1 Solar cell

Solar cells are solid-state devices that convert light energy directly into electricity by photovoltaic effect. By using metallic nanostructured thin films, it is possible to confine and guide incident sunlight into sub-wavelength thickness absorber layer due to the excitation of SPPs or SPRs [1]. Stenzel *et al.* reported an photocurrent enhancement by solar light irradiation with noble metal clusters in a CuPc layer, as a consequence of excitation of SPPs [18]. Brown *et al.* demonstrated a method for enabling SPP-enhanced charge generation in dye-sensitized solar cells, which are entirely compatible with the state-of-the-art processing and technology [21].

1.4.5.2 Chemical and biological sensors

A chemical sensor is a device that transforms chemical information (such as the concentration of a specific sample) into a quantitative signal [1]. SPRs are very sensitive to any change of refractive index at the metal/dielectric boundary and are used in chemical and biological sensors. The main quantities are determined by measuring the change in refractive index of the solution or the chemo-optical transducing medium [59]. In SPR sensors, excitation of SPP can occur if the electric field vector of the light



is parallel to the metal surface, and the momentum between light and the SPP can be matched. These can be achieved by means of prism coupling or grating coupling [32, 39, 60, 61]. In order to quantify the sensitivity of chemical and biological sensors, a figure of merit (FOM) is introduced. FOM is defined as the ratio of the change in resonant wavelength per unit refractive index change and the FWHM of the refractive dip [32]. Recently, Shen *et al.* reported the plasmonic gold mushroom array with perforated gold film approaching the theoretical FOM limit [62].

1.5 Summary

Surface plasmons exist at the interface between metals and dielectrics. The SPRs strongly depends on the shape and size of the nanostructure. The PSPRs and LSPRs can be excited by periodic and isolated metal/dielectric nanostructure respectively. The interactions between two resonances induce CSPR. Moreover, the unique properties of plasmonic fractal nanostructures that have self-similar and space filling geometrical arrangements help to enhance the transmission, resolution and efficiency of sub-wavelength imaging. On the other hand, the position of SPRs can be tuned by temperature instead of changing the shape of nanostructure.

The basic electromagnetic theory of surface plasmons was introduced. Then, the SPRs



based on periodic nanostructure were reviewed. Those SPRs was described by the matching condition equation. Moreover, the theoretical and experimental results of fractal plasmonic nanostructure were summarized. Thermally tunable plasmonic nanostructures were also reviewed. Finally, some applications in surface plasmons were introduced.



Chapter 2

Methodology

2.1 Introduction

This chapter provides an overview of the techniques used in this project, including simulation and experimental methods. It is divided into three sections: simulation method, fabrication techniques and characterization techniques.

2.2 Simulation method

2.2.1 Rigorous Coupled Wave Analysis (RCWA)

In this project, simulations based on the Rigorous Coupled Wave Analysis (RCWA) were conducted using commercial software (DiffractMOD, Rsoft Design Group).

RCWA [63-65] represents the electromagnetic fields as a sum over coupled waves. Fig. 2.1(a) shows the basic simulation structure. In the RCWA method, the simulation structure repeats periodically and infinitely in the x - y plane.

The starting point of DiffractMOD is the Maxwell's equations. For 3D structures or 2D structures with arbitrary shapes, the full vector form of these equations must be taken into account. By factoring out an assumed time harmonic factor $e^{-i\omega t}$, the Maxwell's equations can be expressed as:



$$\frac{\partial}{\partial y} E_z - \frac{\partial}{\partial z} E_y = i\omega\mu H_x \quad (2.1)$$

$$\frac{\partial}{\partial z} E_x - \frac{\partial}{\partial x} E_z = i\omega\mu H_y \quad (2.2)$$

$$\frac{\partial}{\partial x} E_y - \frac{\partial}{\partial y} E_x = i\omega\mu H_z \quad (2.3)$$

$$\frac{\partial}{\partial y} H_z - \frac{\partial}{\partial z} H_y = i\omega\varepsilon_o\varepsilon_{r,x} E_x \quad (2.4)$$

$$\frac{\partial}{\partial z} H_x - \frac{\partial}{\partial x} H_z = i\omega\varepsilon_o\varepsilon_{r,y} E_y \quad (2.5)$$

$$\frac{\partial}{\partial x} H_y - \frac{\partial}{\partial y} H_x = i\omega\varepsilon_o\varepsilon_{r,z} E_z \quad (2.6)$$

where the medium is characterized by a diagonal index tensor with respect to the principle axes with diagonal elements $\varepsilon_{r,x}$, $\varepsilon_{r,y}$ and $\varepsilon_{r,z}$. In order to solve the above equations, the simulation structure is broken into simple building blocks with a vertically homogenous region that there is a single value of dielectric constant in the region (Fig. 2.1(b)) [66]. A periodic permittivity function is represented using Fourier harmonics. Each coupled wave is related to a Fourier harmonic, allowing the full vectorial Maxwell's equations to be solved in the Fourier domain. The diffraction efficiencies are then calculated at the end of the simulations. The spatial field distributions are derived from the Fourier harmonics. In particular, the RCWA method expresses the spatial variations of the refractive index as a Fourier expansion of index as found in slices. Fig. 2.1(b) illustrates the concept. The widths of slices are chosen to

modify the distribution of the refractive index as closely as practical with a minimum number of slices.

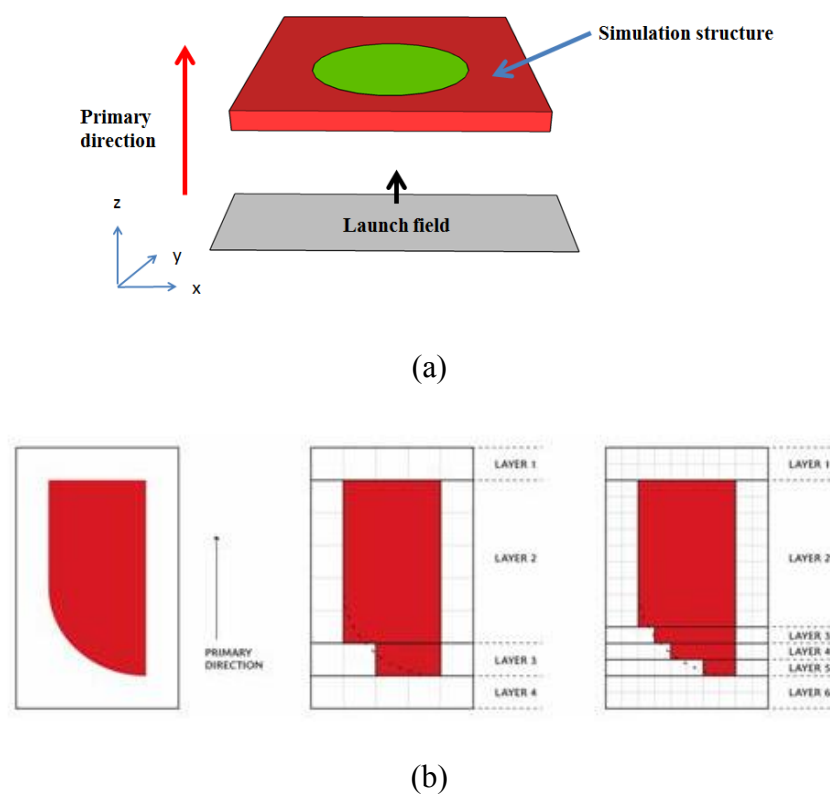


Fig. 2.1 (a) A simple simulation structure and definition of terms (different colors represent different materials). (b) The effect of the index resolution on the simulation layer: the leftmost is original structure, the middle is a coarse index resolution and the rightmost is a fine index resolution [66].



2.3 Fabrication techniques

2.3.1 Soft ultraviolet nanoimprint patterning

In this project, soft ultraviolet nanoimprint patterning was employed to produce periodic nano-pillar structures, which will be discussed fully in Chapter 3.

Typically, photolithography process requires a photosensitive material (photoresist) and a mask that permits the exposure of defined regions to the incident ultraviolet radiation.

Photoresists are categorized into two types: positive type and negative type. The positive resist is removed in the developer solution only for areas that have been exposed to ultraviolet radiation. The negative type photoresist is hardened in the developer solution for regions exposed to ultraviolet radiation.

In most of the imprinting processes, a hard mold is used. However, the use of hard mold may increase the possibility of cracking fragile substrates such as glass or silicon. In this project, soft polydimethylsiloxane (PDMS) molds were used for patterning instead of hard molds. The advantage of soft mold imprinting is that they provide conformal contact with the substrates, so induce a high yield rate for pattern transfer [67].

The imprinting process was carried out in a Class-1000 cleanroom. The original patterns were prepared on quartz master molds by e-beam lithography. The master molds were



coated with a layer of anti-sticking agent of trimethylchlorosilane (TMCS) for easy detachment of the negative PDMS mold [68, 69]. The negative mold was cast from the hard master by mixing silicone elastomer and the curing agent (Sylgard™ 184) at a weight ratio of 10:1 and baked at 65°C for 2 hours. After hardening, the soft PDMS molds were treated with TMCS.

Fig. 2.2 shows the imprinting procedures. Firstly, poly(methyl methacrylate) (PMMA) and a negative nano-imprint resist (Amonil) were spun on the substrates at 2000 and 7000 rpm respectively for 30 seconds, producing 300 nm-thick PMMA and 150 nm-thick Amonil on glass substrates; different heights of nano-pillars can then be achieved due to different etching rates of PMMA and Amonil. This was followed by UV exposure (450 W and 360 seconds) while the resist layers were imprinted with PDMS molds with suitable patterns. After solidification, the PDMS mold was detached from the sample.

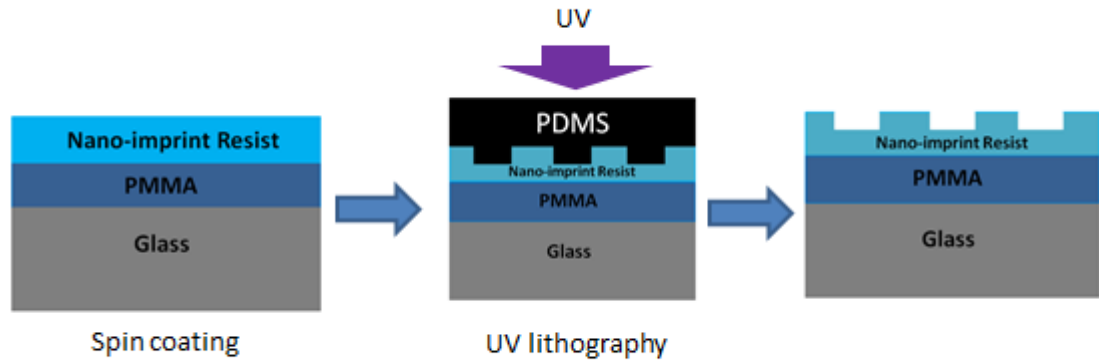


Fig. 2.2 Soft ultraviolet nanoimprint patterning procedures for preparing patterns on nano-imprint resist.

2.3.2 Inductive coupled plasma (ICP) etching

Inductively coupled plasma (ICP) is a type of plasma source in which the energy is supplied by electric currents which are produced by electromagnetic induction, that is, by time-varying magnetic fields [70]. The ICP etching system makes use of the inductively coupled plasma technique that can generate high-density plasma at low pressure. With the decoupling of the plasma density and ion energy, many ions with low ion energies can be produced at low pressures. As a result ion bombardment damage can be kept low while maintaining high etching rates and good anisotropic etching.

ICP etching was used to adjust the height of the periodic plasmonic nano-pillars. The



dual layer shown in Fig. 2.2 can generate different heights of dielectric pillars because of different etching rates of PMMA and Amonil. The etching rate of PMMA layer in the ICP system with oxygen plasma (1Pa and 60 sccm), 630 nm/min as obtained with a sample bias power of 30 W and radio frequency power of 200 W, was about 10 times higher than that of Amonil [71].

2.3.3 D.C. magnetron sputtering

Sputtering is one type of physical vapor deposition techniques, which allows different materials (metals, oxides and semiconductors) to be deposited [72, 73] . A DC magnetron sputtering system was used for the gold deposition, because of its ability to produce high-quality films with uniform thickness over a large area; the schematic diagram of the D.C. magnetron sputtering system used in my project is shown in Fig. 2.3. The deposition process was conducted in an ultrahigh vacuum chamber. Substrates were placed on a substrate holder, which was rotated at a constant speed (~ 1 rpm) during the sputtering process to promote uniform film deposition. A high negative potential was applied to the target to produce an electric discharge while the substrate holder was grounded. During the sputtering process, argon gas was introduced for plasma generation, with the pressure being closely monitored. The magnetic field

produced by the magnetron was used to trap electrons into a helical path close to the surface of the target. This increased the probability of ionizing neutral Ar gas. Under the influence of an electric field, argon ions bombarded the target surface and neutral atoms of target were removed, which travelled towards the substrates and achieved the material deposition process [72, 73].

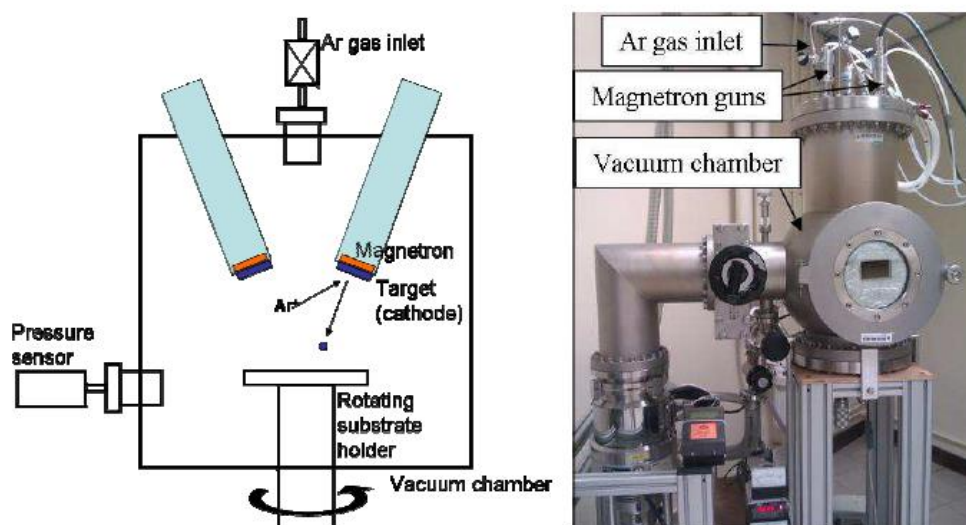


Fig.2.3 Schematic diagram (a) and the actual setup (b) of the D.C. magnetron sputtering system used in this work.

The sputtering technique was used to prepare metallic coatings on periodic nano-pillars (Chapter 3) and grating (Chapter 5) in this work experimentally. The sputtering system was pumped down to a pressure of 1×10^{-4} Torr or better. After reaching the high vacuum level, a Au layer was deposited onto the specimen at room temperature with an



Ar pressure of 1.6×10^{-3} Torr. The Au was sputtering at 70 W, and the thickness of Au layer was 25 nm.

2.4 Characterization techniques

2.4.1 Scanning electron microscope (SEM)

Scanning electron microscopy (SEM) is a high-resolution imaging technique that makes use of a high-energy electron beam to scan over the sample surface for producing images of the sample, including surface topography, cross-section image and thickness.

An electron beam is emitted from a field-emission cathode and then accelerated by an anode and focused by electromagnetic lenses to the sample surface. Upon interactions between the electron beam and the sample, Secondary electrons and backscattered electrons are generated and contribute to the formation of images [74]. All SEM images presented in the project were obtained with a JEOL JSM-6335F field emission scanning electron microscope (FE-SEM).

2.4.2 Atomic force microscope (AFM)

Atomic force microscope (AFM) is one kind of scanning probe microscopes that can provide information on the two-dimensional topography of a substance and has a resolution down to the nanometer scale. As shown in Fig. 2.4, when a cantilever scans



over a surface, attractive and repulsive forces between the surface and the tip lead to the deflection of the tip; a laser beam illuminating on the backside of the tip is reflected from the cantilever, and the signal is detected.

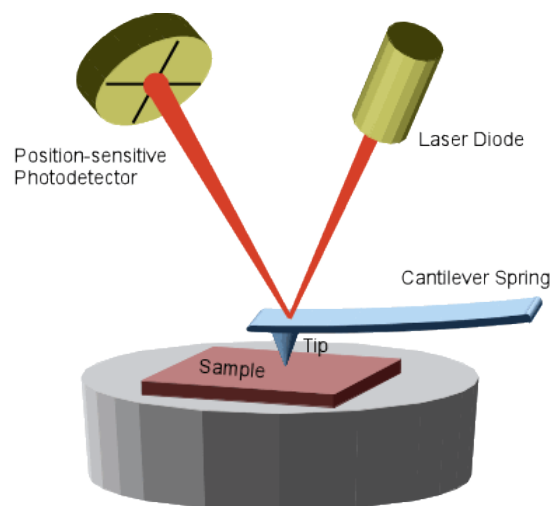


Fig. 2.4 Schematic of the major components of an AFM. [10].

Tapping mode AFM is commonly used as the tip does not scratch the sample directly, and therefore it is non-destructive to the samples. In the tapping mode, an AC voltage is applied to the piezoelectric scanner which is composed of a cantilever and a tip. When the tip vibrating near its resonant frequency is scanned over the surface of a sample, attractive and repulsive forces are experienced by the tip when the tip is further apart or too close to the surface. The change of distance between the sample and the tip induces a frequency shift to the cantilever. This change can be detected by the laser and the laser



beam is reflected to the mirror, reaching the detector. These signals are converted into graphical image, representing the topography of the sample [75, 76].

AFM can be used for scanning the topology of samples composed of metal, semiconductor and insulator without sample preparation. It allows scanning for surface morphology and produce three-dimensional images with the aid of software. The AFM images presented in this project were captured with a Digital Instruments Nanoscope VIII AFM.

2.4.3 Ultraviolet–visible spectroscopy

Transmittance of the specimens was measured by a Shimadzu UV-2100PC UV-VIS scanning spectrophotometer (Fig. 2.5). The spectrophotometer has a broadband light source of wavelength ranged from 200 to 900 nm. The transmittance T can be calculated by the ratio of transmitted intensity I to incident intensity I_0 ,

$$T = \frac{I}{I_0} \quad (2.7)$$



Fig. 2.5 Ultraviolet–visible spectroscopy used in this work

2.4.4 Angular dependent reflectivity

The angular-dependent reflectivity was measured by a computer-controlled goniometer equipped with a charge-coupled device detection system [77]. During the measurement, *p*-polarized light was collimated and incident on the sample in a plane perpendicular to the nano-pillar and grating (as introduced in Chapters 3 and 5). The reflection spectra from 600 to 1100 nm were recorded at incident angles from 5° to 60° with a step size of 0.5°, and the results were normalized with respect to the incident light spectrum. The measurement system is shown in Fig. 2.6.

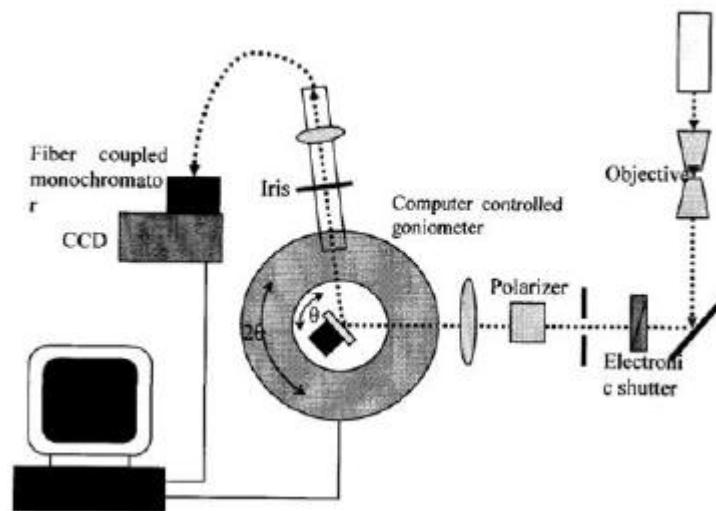


Fig. 2.6 Schematic diagram of the visible range angular-dependent reflection measurement system [78].

2.5 Summary

To summarize, the background and mechanism of RCWA simulation were described. Details of fabrication technique were revealed, including soft ultraviolet nanoimprint patterning, ICP etching and DC magnetron sputtering. In the last session of the chapter, the characterization techniques involved such as FE-SEM, AFM and angular dependent reflectivity were introduced.



Chapter 3

Optical analysis of periodic plasmonic nano-pillars

3.1 Introduction

Surface plasmons are coherent oscillations of electrons at metal-dielectric interfaces that can exist in propagating and localized forms [79-81]. The optical responses of the device structures such as reflectivity, transmittance and electric field intensity enhancement of incident waves) depend on the geometry and spatial arrangement of the constituent features [42], and hence the feature dimensions play pivotal roles in the design of device structures based on surface plasmon resonance effects.

Propagating surface plasmon resonances (PSPRs) are evanescent electromagnetic waves bounded by flat and smooth metal-dielectric interfaces, which result from oscillations of the conduction electrons in the metal [82]. Localized surface plasmon resonances (LSPRs) are non-propagating excitations of the conduction electrons in metallic nanostructures coupled to the electromagnetic waves [81]. LSPRs cause highly-localized electromagnetic fields outside the nanoparticles [83]. Such SPR-based structures have potential for applications in biological sensing, refractive index sensing



and antennas [32, 84, 85].

Recently, two-dimensional arrays of plasmonic gold nano-pillars, which consist of dielectric nanopillars with gold caps and standing within a perforated gold film, were found to possess a very high figure of merit (FOM), which is an important parameter for comparing the performance of sensing devices [32]. The perforated gold film supports PSPRs and the gold caps support LSPR modes. In such a capped-nanopillar structure, new plasmon resonance modes due to coupling between PSPRs and LSPRs were obtained [62]. However, the effect of the height of nano-pillars was not investigated. As the pillar height varies, the gold layer changes from a continuous film to two discontinuous parts (gold caps on nanopillars, and the perforated gold film), with the corresponding transition from a purely PSPR (for pillar height equals to zero) to two independent SPR modes (for pillar height much larger than gold film thickness). It is worthwhile to study the evolution of the coupling effect with different heights of nano-pillars.

In this part of the M.Phil. project, nano-pillar structures with gold caps and perforated gold film at the base of the pillars were investigated numerically and experimentally.

The reflectivity and electric field intensity distribution of the structure were calculated



and measured in the visible to near-infrared ranges (300 – 3000 nm). It was shown that the PSPRs and LSPRs appeared in the structure simultaneously and induced coupled surface plasmon resonance (CSPR) modes. It was also shown that PSPRs were independent of the heights of the pillars, but was dependent on the incident angle of light. On the other hand, CSPRs were dependent on the heights of the pillars but independent of the incident angles. Moreover, at the reflection dip of CSPR, the electric field was confined along the surfaces of the dielectric nano-pillars, at the air-dielectric interface.

3.2 Fabrication of periodic plasmonic nano-pillars

Two-dimensional (2-D) periodic arrays of nano-pillars were fabricated on glass substrates using nanoimprint lithography, followed by gold film deposition using sputtering or e-beam evaporation. The fabrication process is simple and cost-effective, which is beneficial for practical device fabrications.

Firstly, poly(methyl methacrylate) (PMMA) and nanoimprint resist (Amonil) were spun on glass substrates at 2000 and 7000 rpm respectively for 30 seconds, producing 300-nm thick PMMA and 150-nm thick Amonil on the substrates. This dual layer can generate different heights of dielectric pillars because of the difference in etching rates.



This was followed by UV exposure (450 W and 360 seconds) while the resist layers were imprinted with polydimethylsiloxane (PDMS) molds with square lattice arrays of holes, during which the nanoimprint resist was cured. This produced periodic nano-pillars with 200-nm diameter and 400-nm periodicity in square lattices. Finally, a 25-nm thick Au film was deposited (Fig.3.1). The height of nano-pillars was controlled by ICP etching time.

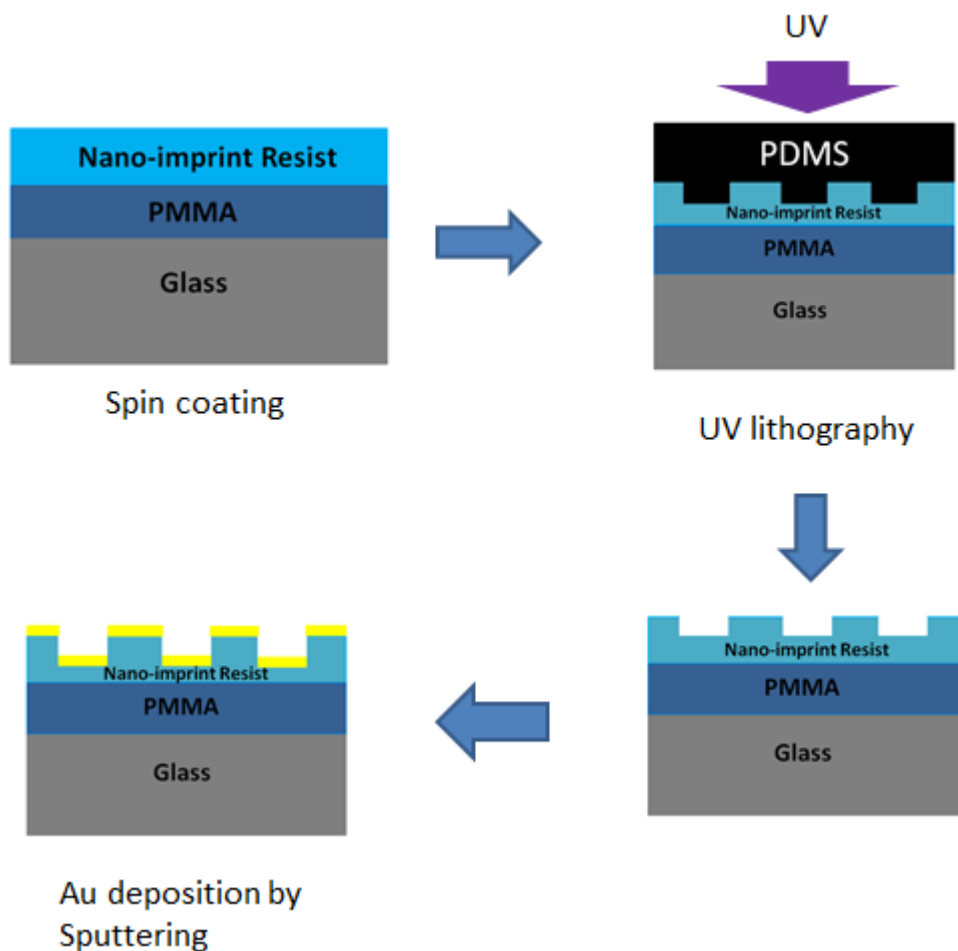


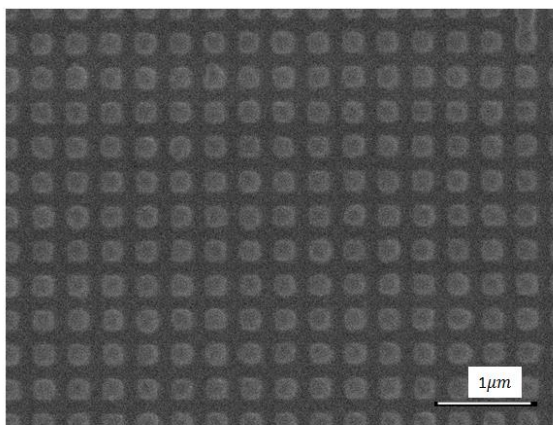
Fig.3.1 Schematic of the process flow for sample fabrication.



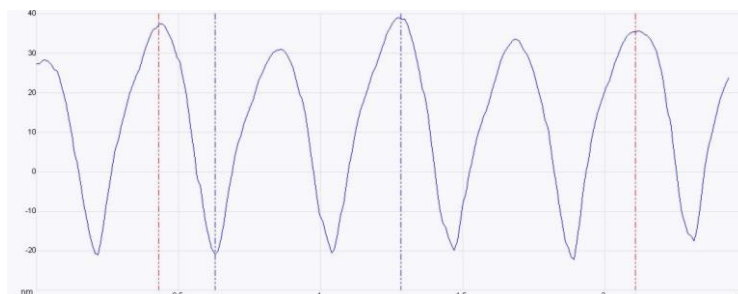
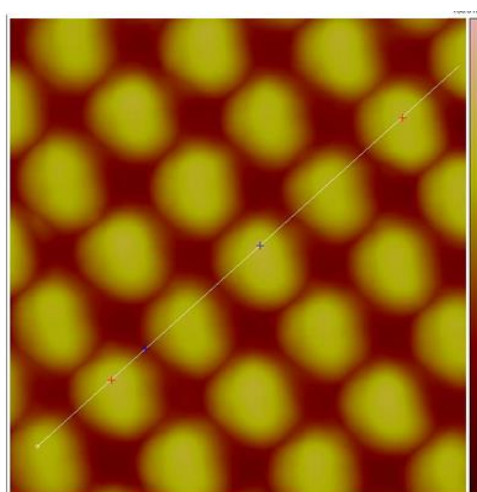
3.3 Characterization of periodic plasmonic nano-pillars

3.3.1 Structural characterization of periodic plasmonic nano-pillars

Fig. 3.2(a) shows the scanning electron microscopy (SEM) image of a square periodic array of plasmonic nano-pillars. The diameter of the pillars is around 200 nm, with a periodicity of 400 nm. Fig. 3.2(b) shows an atomic force microscopy (AFM) image of the structure. The measured height of nano-pillar is about 60 nm.



(a)



(b)

Fig. 3.2 (a) Top view of the SEM image of periodic plasmonic nano-pillars. (b) AFM image and sectional profiles of periodic nano-pillars.



3.3.2 Optical characterization of periodic plasmonic nano-pillars

In this project, the angular reflectivity of the samples was measured by means of a computer-controlled goniometer equipped with a charge-coupled device detection system [77]. During the measurement, transverse magnetic (TM)-polarized light was collimated on the sample with different incident angles. Fig. 3.3 shows the simulated and measured reflection dispersion relationship of 70-nm high nano-pillars. Results in Fig. 3.3(a) and (b) show simulated and measured Au/air (1,0) and Au/Amonil(1,0) PSRPs, respectively, which will be discussed in the next part.

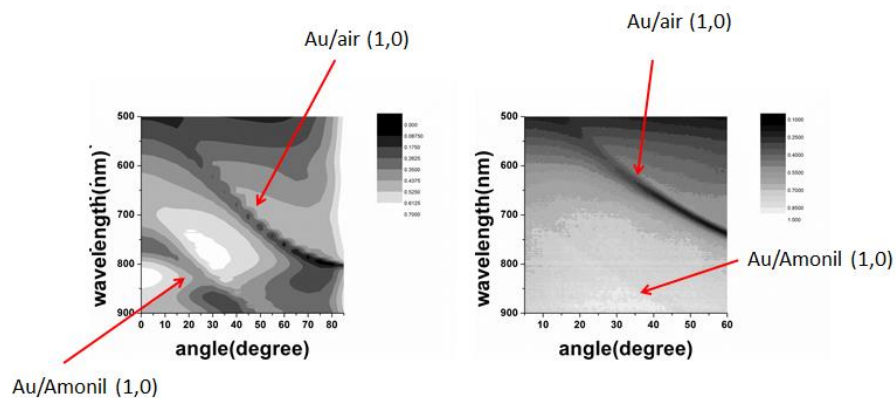


Fig. 3.3 (a) Simulated and (b) measured angular dispersion relationships of periodic plasmonic nano-pillars with 70 nm-tall pillars. TM-polarized light was used in the calculations and measurements.



3.4 Theoretical study of periodic plasmonic nano-pillars

3.4.1 Numerical simulation

The nano-pillars structure studied in this work were based on the two-dimensional (2-D) periodic metal/dielectric system. The schematic diagram of the nanostructure is shown in Fig. 3.4. The nanostructure consists of gold caps on dielectric pillars, which in turn stand within a perforated gold film. Nano-pillars of photoresist (refractive index $n = 1.51$) are arranged in a square array and are placed on top of a glass substrate ($n_{sub} = 1.5$). The diameter and periodicity of the pillars are 200 nm and 400 nm, respectively. A layer of 25 nm-thick gold film is then ‘deposited’ on the top of the nano-pillars, as well as in the regions between the pillars on the base. It should be noted that there is no gold at the sidewall in this structure; this can be achieved experimentally by exposing the patterned dielectric film normally to the plasma of incoming adatoms. Theoretically, these two layers are disconnected if the height H of the pillars is larger than the thickness of the gold film. The thickness of gold film in this investigation was kept at 25 nm, and the glass was treated as semi-infinite in our analysis. Due to the absence of surface plasmon mode for transverse-electric (TE) polarization, I only considered TM-polarized light with normal incidence in this investigation. The incident wave was



launched from air. The material database of DiffractMod of RSoft™ [86] was adopted for the simulation of dielectric properties of gold, based on the combined Drude and multiple Lorentzian model [87]:

$$\varepsilon_r(\omega) = 1 - \omega_p^2 / \omega^2 \quad (3.1)$$

where ε_r is the dielectric constant, ω_p is the plasma frequency of gold in the free electron model. The harmonic and the refractive index resolution used in RCWA of DiffractMOD™ were 10 and 0.00312 respectively.

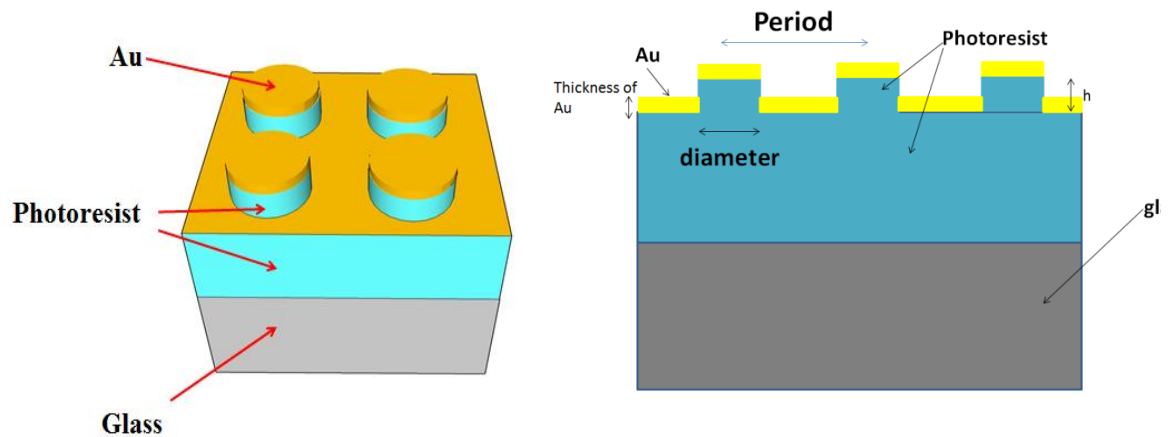


Fig. 3.4 Schematic of isometric view (a) and cross-sectional view (b) of the simulation model.



3.4.2 Influence of height of periodic plasmonic nano-pillar on reflection spectra and electric field intensity distribution

As shown in Fig. 3.5, when the height of nano-pillars increases gradually, the gold film changes from a continuous layer (Fig. 3.5(a)) to disconnected entities of gold caps and perforated gold film on the substrate (Fig. 3.5(b)). Fig. 3.6 shows the simulated reflectivity spectra of periodic plasmonic nano-pillars. When the height of the pillars is less than the thickness of gold (i.e. a continuous gold film), there is not reflectivity dip in the simulated reflection spectra. In contrast, reflection dip can be observed when the height of pillars is larger than the thickness of the gold layer.

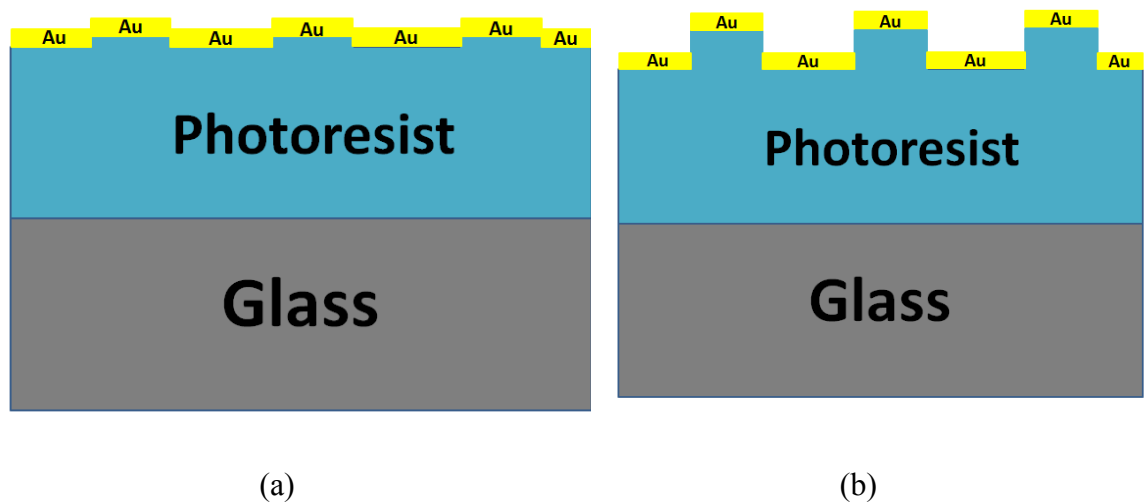


Fig. 3.5 Side view of periodic plasmonic nano-pillars with height less than (a) and larger than (b) the gold layer thickness.



To identify the nature of the reflection dips, the electric field intensity distribution was simulated for the pillar height of 40 nm. Simulation results show that electric field is concentrated along the length of the pillar, as shown in Fig. 3.7. However, surface plasmon effect is not induced at the air-dielectric interface because surface plasmon should be induced at the interface between metal and dielectric. Therefore, there is only one possible reason for this dip which is caused by CSPR.

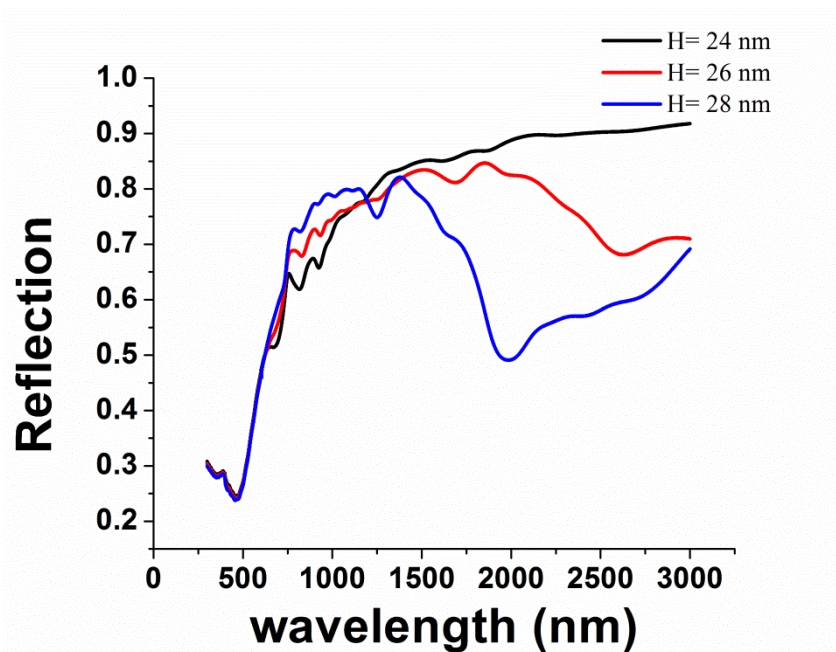


Fig. 3.6 Simulated reflectivity spectra of periodic plasmonic nano-pillars with different heights ($H= 24$ nm, 26 nm and 28 nm).

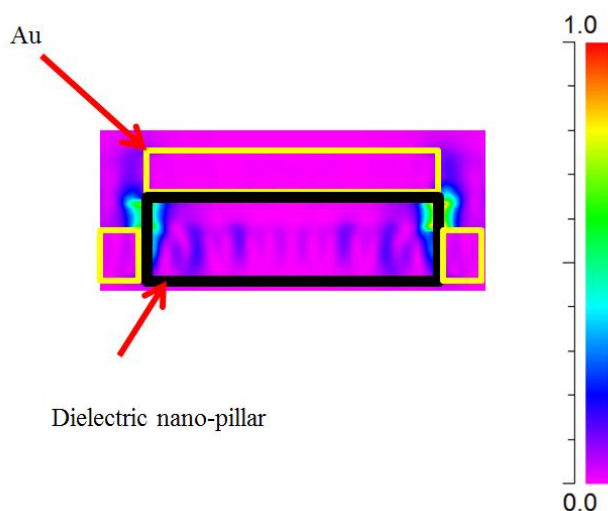


Fig. 3.7 Electric field intensity distribution of the periodic nano-pillar with $H = 40$ nm at the reflection dip of wavelength = 1889 nm, normalized to the maximum field intensity. The maximum field intensity enhancement factor under such a condition is 492.

Fig. 3.8 shows the simulated reflection spectra with different heights H of periodic nano-pillars. There are two types of dips in the near infrared region, which are labelled D1 and D2 in the figure. D1 red-shifts linearly with increasing height of nano-pillars (Fig. 3.9). On the other hand, the resonant wavelengths of D2 dips drop exponentially with increasing height of nano-pillars (Fig. 3.10). For different heights of nano-pillars, Fig. 3.11 show the simulation results that at the reflection dips D1 the electric field is concentrated at the edges of the top gold caps. This proves that D1 is a LSPR mode of



the nano-disk. On the other hand, Fig. 3.12 shows the normalized electric field distribution with different height of nano-pillar at the reflection dip D2. The electric field is generally located along the lengths of the nano-pillars, at the interface between air and nano-imprint resist. Therefore, D2 dips are caused by the coupling between resonant modes around the upper gold caps and the lower perforated gold film, which are termed as coupling surface plasmon resonances (CSPRs) in this thesis. When the height of the nano-pillars is increased, the coupling effect becomes weaker due to the increase in separation between the top gold cap and the perforated gold film.

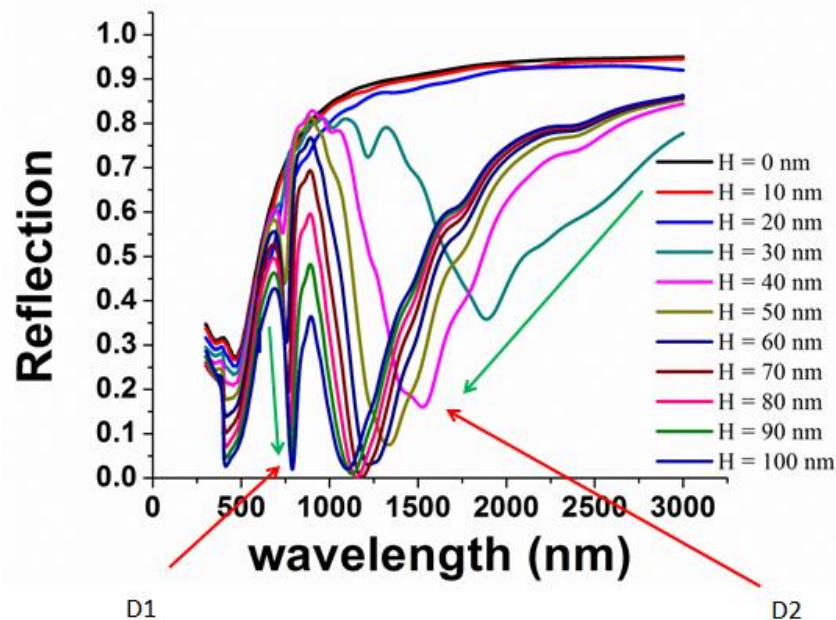


Fig. 3.8 Simulated reflection spectra with different heights of nano-pillars from $H = 0$ (continuous gold film) to $H = 100$ nm. D1 is a LSPR and D2 is a CSPR reflection dip.

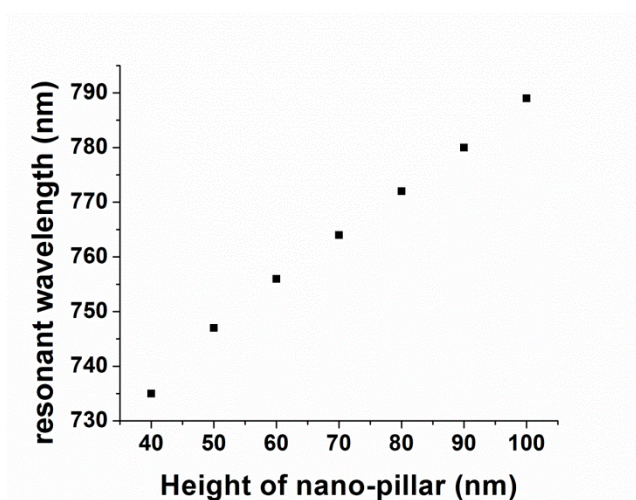


Fig. 3.9 Simulated reflection dip D1 with different heights of periodic nano-pillars.

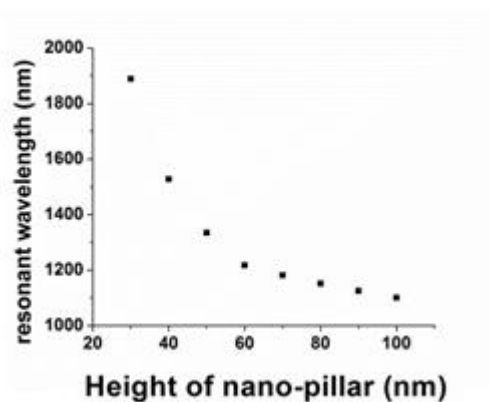


Fig. 3.10 Simulated reflection dip D2 with different heights of periodic nano-pillars.

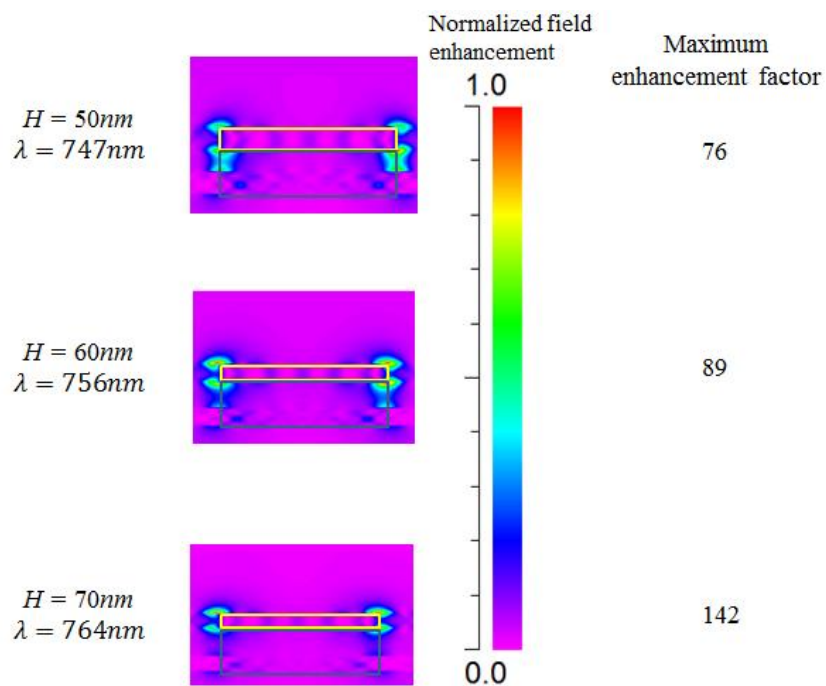


Fig. 3.11 The electric field intensity distribution at reflection dip (D1) with different heights of nano-pillars. The maximum electric field intensity of incoming wave is normalized to 1.

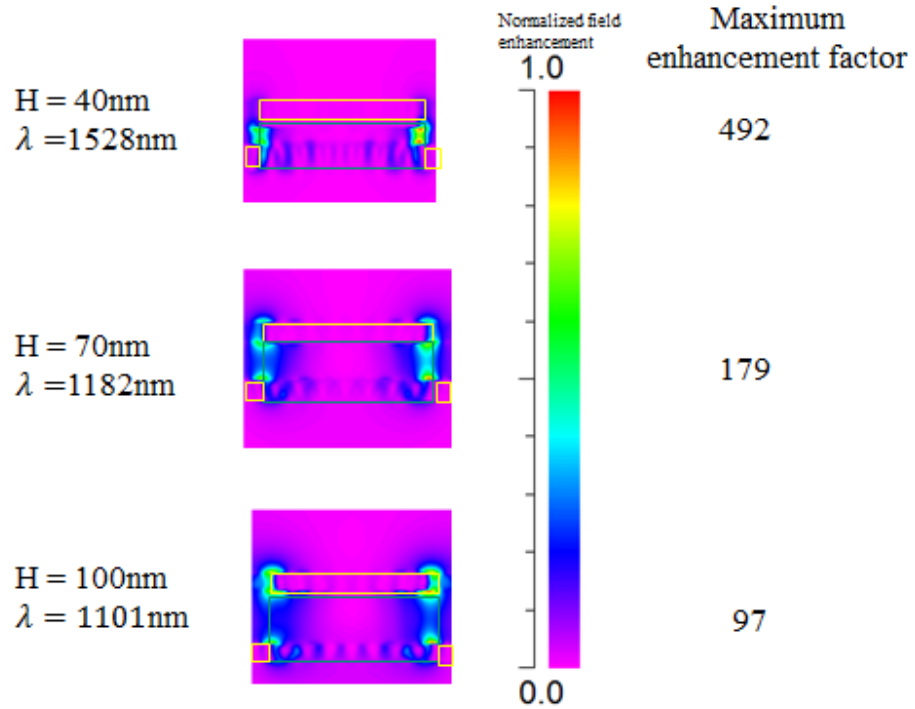


Fig. 3.12 The normalized electric field intensity distribution at the reflection dip (D2) with different heights of nano-pillars.

In order to further investigate CSPR and PSPR, the simulated dispersion relationship of reflectivity with 50 nm-tall periodic nano-pillars was obtained and is shown in Fig.

3.13. For a square lattice, the matching condition between PSPR and the in-plane wave vectors of the incident light is given by:

$$\mathbf{k}_0 \sin \theta \pm i\mathbf{G}_x \pm j\mathbf{G}_y = \mathbf{k}_{\text{mode}} \quad (3.2)$$

Where \mathbf{k}_0 is the wave vector of the incident light at a polar angle θ , \mathbf{G}_x and \mathbf{G}_y are the Bragg vectors associated with the two periodicities in x- and y-directions of the array,



and i and j are integers indicating the order of the scattering events that couple to the incident light with vector \mathbf{k}_{mode} [39], \mathbf{k}_{mode} is the wave vector of a specific mode of the structure given by:

$$\mathbf{k}_{\text{mode}} = \mathbf{k}_0 \sqrt{\frac{\epsilon_m \epsilon_d}{\epsilon_m + \epsilon_d}} \quad (3.3)$$

where ϵ_m and ϵ_d are the dielectric constants of metal and dielectric (nanoimprint resist in this case), respectively.

Based on the above equations, Au/Air (1,0) and Au/Amonil (1,0) PSPR modes are identified in Fig. 3.13, and these PSPRs are red-shifted with increasing incident angle.

According to the electric field intensity distribution, the dip D2 is known as CSPR, which is independent of the incident angle. Fig. 3.14 shows the normalized electric field intensity distribution of the 3 dips for 50 nm-tall nano-pillars, at an incident angle of 40° . It should also be noted that the electric field intensity enhancement factor is the largest in the CSPR.

On the other hand, Fig. 3.15 shows the reflection spectra with different heights of periodic nano-pillars at an incident angle of 40° . Two of the dips are identified as PSPR of Au/Air (1,0) and Au/Amonil (1,0) respectively, according to the matching condition



equation. The dip positions of PSPR are independent of the height of the nano-pillars. On the other hand, the D2 dip positions are the same with different incident angles. In contrast, CSPR is dependent on the height of nano-pillars. Also, simulations show that at wavelength of dip D2, the electric field is located at the surrounding of the nano-pillar, which is the gap between top gold layer and lower perforated gold film.

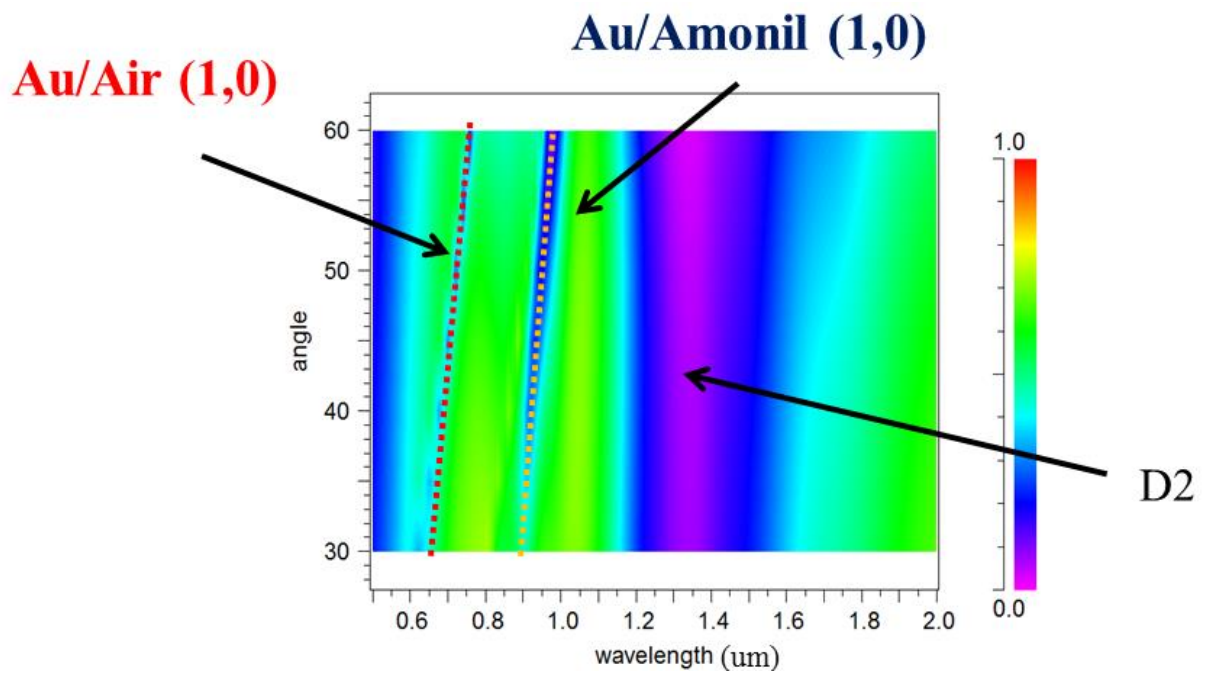


Fig. 3.13 Reflection dispersion relationship with $H = 50$ nm.

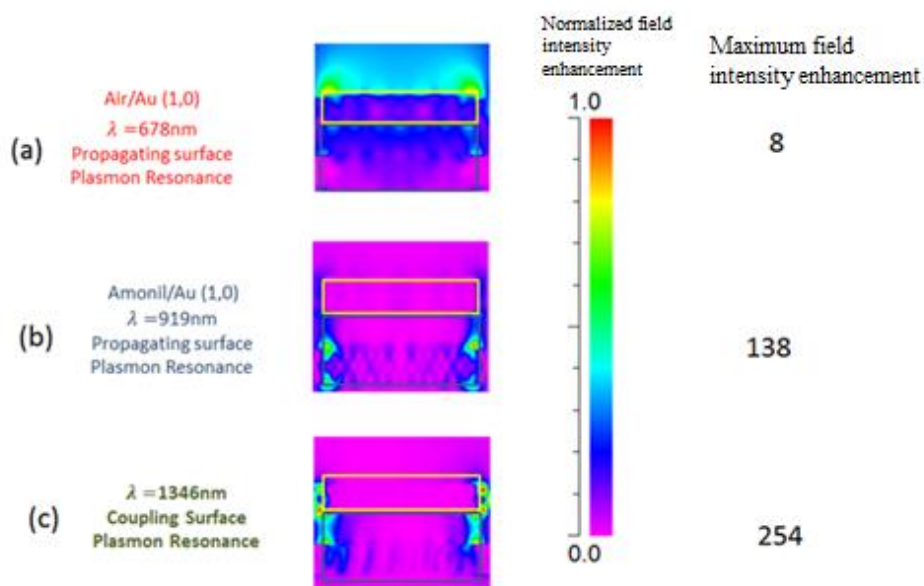


Fig. 3.14 Normalized electric field intensity distribution at different resonance modes:

(a) Au/air (1,0), (b) Au/Amonil(1,0) and (c) CSPR.

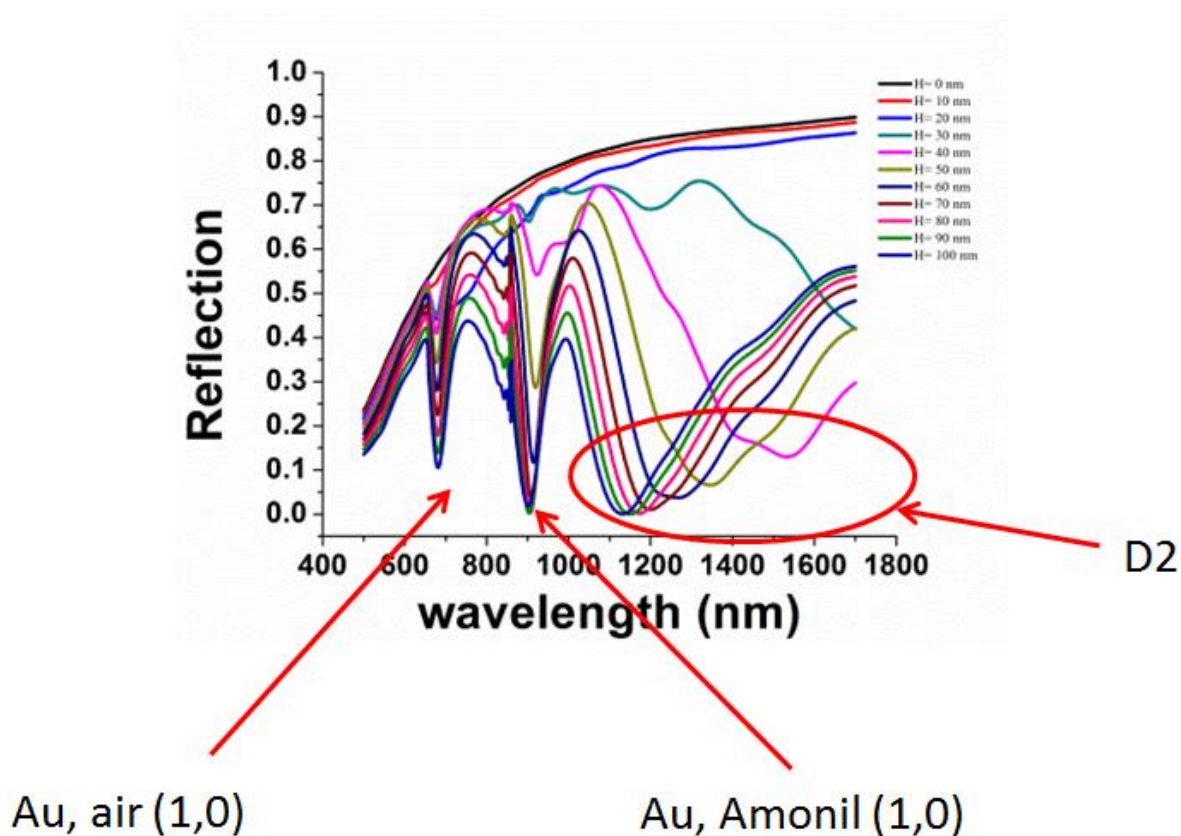


Fig. 3.15. Reflection spectra with different heights of nano-pillars at incident angle = 40°

3.5 Application of periodic plasmonic nano-pillars

The full optical analyses of periodic plasmonic nano-pillars were reported above. One of the applications of periodic plasmonic nano-pillars is refractive index sensing. In this section, the comparative parameters of refractive index sensing are demonstrated.



3.5.1 Refractive index sensor

Confined to a metal/dielectric interface, surface plasmons are known to be extremely sensitive to the refractive index of the dielectric medium. Hence, this property is used in refractive index sensing and biosensing, which emerges as a leading modern technology for detection and studies of binding events between target analytes and their corresponding receptors on metal surfaces [29, 32, 84, 88, 89]. The figure of merit (FOM), which is defined as the refractive index sensitivity (nm/RIU) divided by full width at half maximum (FWHM) of plasmons resonance dip, is used to determine the degree of sensitivity of nanostructures for refractive index sensing [32].

Fig. 3.9 shows that the two reflection dips D1 and D2 are linearly red-shifted and exponentially blue-shifted with the height of nano-pillars respectively. D1 is more suitable to be used for refractive index sensing because it is easier to tune the resonant wavelength by changing the height of pillars. Also, D1 is narrower than D2, so the FWHM of D1 dip is lower than that of D2. Hence, the FOM of D1 is higher than D2. The FOM achieved us 8.86 and 0.704 at D1 and D2 from the simulation results respectively. The FOM of D2 is much smaller than that of D1.

Fig. 3.16 shows the reflection spectra around the PSPR Au/Amonil (1,0) dip, with



different refractive index from 1.33 to 1.4, at $H = 50$ nm and incident angle of 50° .

There is a linear relationship between the resonant wavelength and the refractive index,

the sensitivity is calculated as 400 nm per unit refractive index. The FOM of PSPR

Au/Amonil(1,0) achieved is 8.53, which is slight lower than FOM of D1. In summary,

dip D1 is more suitable to be used in refractive index sensing in the periodic nano-

pillars.

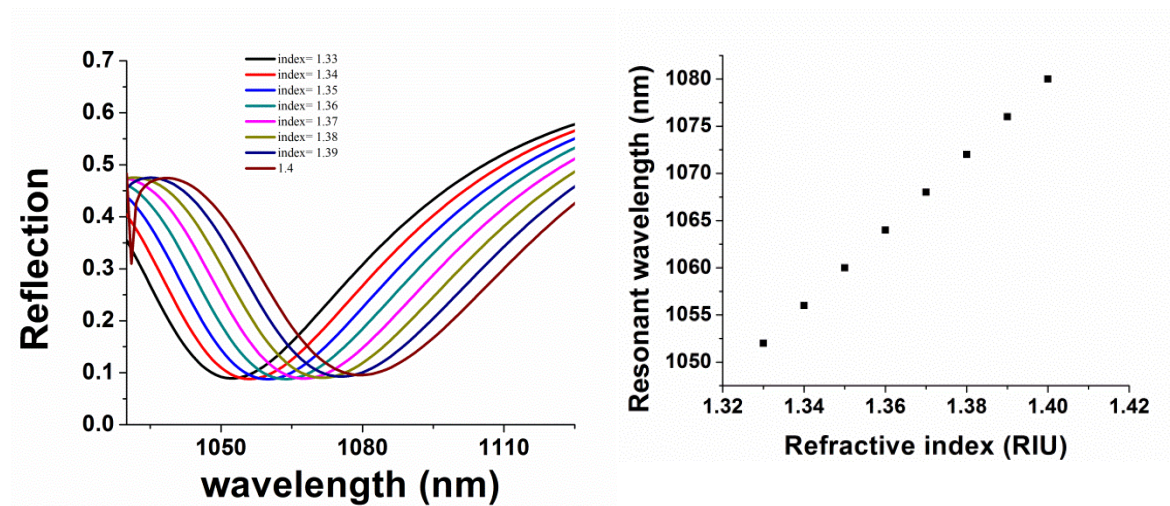


Fig. 3.16 (a) Simulated reflection spectra of the periodic plasmonic nano-pillars with different refractive indices at the angle of 50° and $H = 50$ nm. (b) The relationship between resonant wavelength and refractive index at the angle of 50° and $H = 50$ nm.

3.6 Summary

I introduced a periodic plasmonic nano-pillar structure and investigated the interaction between the top gold layer and bottom perforated gold film. These interaction between



the two systems induced CSPR, with the incident wave confined at the surrounding of the nano-pillars. The resonant wavelength of CSPR is reduced with the height of the nano-pillar exponentially. In particular, the electric field intensity enhancement became weaker with increasing height of nano-pillars. Besides, PSPRs appeared at the same nanostructure, and the dip positions of PSRPs were independent of the height of nano-pillars but dependent on the incident angle. In contrast, dip positions of CSPR were dependent on the height of nano-pillars but independent of the incident angle. The periodic plasmonic nano-pillar structure can be used for refractive index sensing.



Chapter 4

Analysis of plasmonic Center Fractal pattern

4.1 Introduction

Recently, the influences of fractal iterations (such as Sierpiński triangles [90, 91] and H-shaped fractals [92-94]) on the surface plasmon resonance behavior were investigated in the near- to mid- infrared regimes. Fractal is a structure made of patterns which are similar to the whole structure in some way iteratively [43]. The resulting structures exhibit special properties, such as simultaneous zero and infinite perimeters [95]. This concept is used in the design of fractal plasmonic structures, which have self-similar and space-filling geometric arrangements that can result in some interesting electromagnetic properties [45, 95].

Self-similar properties of the fractal are translated into its electromagnetic behavior [46, 47]. It has been demonstrated that nanoscale fractal apertures allow for enhanced transmission and resolution for near- to mid- infrared wavelengths [48, 96]. For example, there is a larger perimeter-to-footprint ratio in higher-order fractal structures as compared with the basis shape, causing red-shifted resonance conditions [95].

Besides, the fractal plasmonic structure can increase the metal/dielectric interface area



with increasing order of the fractal. This can help to control the spatial distribution of the electric field in the structure. Finally, there is potential for the fractal nanostructures to be used in different applications such as biosensing, antennas and solar cells. [97, 98].

In this Chapter, a type of fractal plasmonic nanostructure, in which the fractal pattern is self-similar to the central part of the structure, is investigated theoretically. The reflection and transmission properties, as well as the electric field intensity distribution of the fractal nanostructure, were calculated in the visible light and the near- infrared range (400 – 2300 nm) by the Rigorous Coupled-Wave Analysis (RCWA) method, using a commercial software (DiffractMod of RSoft™) [99]. It was shown that the proposed fractal nanostructure can help to confine and enhance the incident waves at the center of the unit nanostructure. High intensity enhancement factors in the proposed fractal nanostructure can improve the sensitivity of the biosensing for real-time detection of different proteins [29, 32, 88, 89]. Also, properly-designed nanostructures are known to produce so-called hot spots to enhance the incident electromagnetic waves. The efficiencies of sensitive physical process and confinement factor are also enhanced. The plasmonic resonances observed in the center fractal structure open the



possibility to build antennas for radiating and receiving electromagnetic energy [87, 95, 100-105].

4.2 Theoretical study of plasmonic Center Fractal

4.2.1 Simulation model

The fractal nanostructures studied in this part of the project are based on the Au film/glass substrate metal/dielectric system. The fractal patterns are shown in Fig. 4.1

The starting structure is a Au square of edge length l_0 . The square is then divided into 9 equal-sized squares (edge length $l_0/3$) and the central square is removed; this configuration is the order 1 pattern. The removed square is further divided into 9 equal-sized squares (edge length $l_0/9$) and the center is filled with Au again (order 2 pattern).

The same procedure is repeated for higher orders, with the smallest square having an edge length of $l_0/3^n$, where n is the order of the fractal pattern. The smallest square is empty or filled, depending on whether the order of the pattern is odd or even. Fig. 4.1(a) shows the first 3 orders of fractal nanostructures studied in this chapter. This is in contrast with the Sierpiński carpet (Fig. 4.1(b)), which starts with a square of side length l and is then divided into a (3 x 3) grid of $l/3$ -sided squares and the central sub-square is removed. In the pattern studied in this chapter, the self-similar squares appear

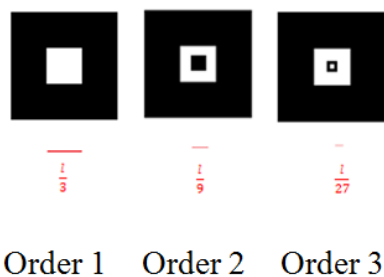


only in the center of the structure, and the pattern is called “center fractal” in this thesis.

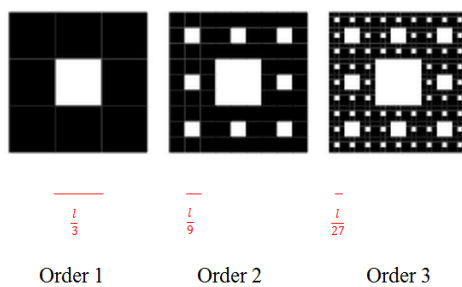
The proposed structure consists of a 2-D periodic fractal pattern in a Au film, which is placed on top of a glass substrate with refractive index $n_{sub} = 1.5$. The schematic is shown in Fig. 4.1(c). The geometry of the center fractal nanostructure can be fully described by the periodicity of the basic unit P , the length of the basic unit l_o and the fractal order n . The thickness of the Au film in this investigation is kept at 25 nm, and the glass is treated as semi-infinite in the analysis. Transverse-magnetic (TM) polarized light is considered with normal incidence in this project. In this study, the incident wave is launched from air. The material database of DiffractMod of RSoft™ [99] was adopted for the simulation of dielectric properties of gold, based on a combined Drude model and multiple Lorentzian models:

$$\varepsilon(\omega) = 1 - \omega_p^2 / \omega^2 \quad (4.1)$$

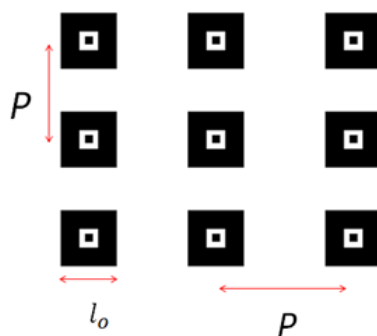
where ε is the dielectric constant, ω_p is the plasma frequency of gold in the free electron model [87].



(a)



(b)



(c)

Fig. 4.1 Schematic of the first three orders of the (a) center fractal pattern and (b) Sierpiński carpet. (c) Schematic of periodic fractal pattern nanostructure. The black regions represent gold and white areas correspond to air.



4.2.2 Influence on electric field intensity distribution with different structural parameter (periodicity and order) and compare with Sierpiński Carpet

For the same fractal order n , simulation results show that as the periodicity P increases from l_o to $10l_o$, the maximum electric field intensity enhancement factor decreases. For example, at an incident wavelength $\lambda_o = 800$ nm, $l_o = 1$ μm and order $n = 1$, the maximum electric field intensity enhancement factor ($|E|^2/|E_o|^2$) for each basic unit of the nanostructure are 5.38, 1.75 and 0.686 for $P = l_o$, $5l_o$ and $9l_o$, respectively (Fig. 4.2).

This shows that the interaction among the basic units is weakened with increasing P . In order to maximize the electric field intensity enhancement of the nanostructures, P is set equal to l_o (edge length of the basic unit) in the following investigation, which is equivalent to a continuous Au layer with periodic fractal patterns.

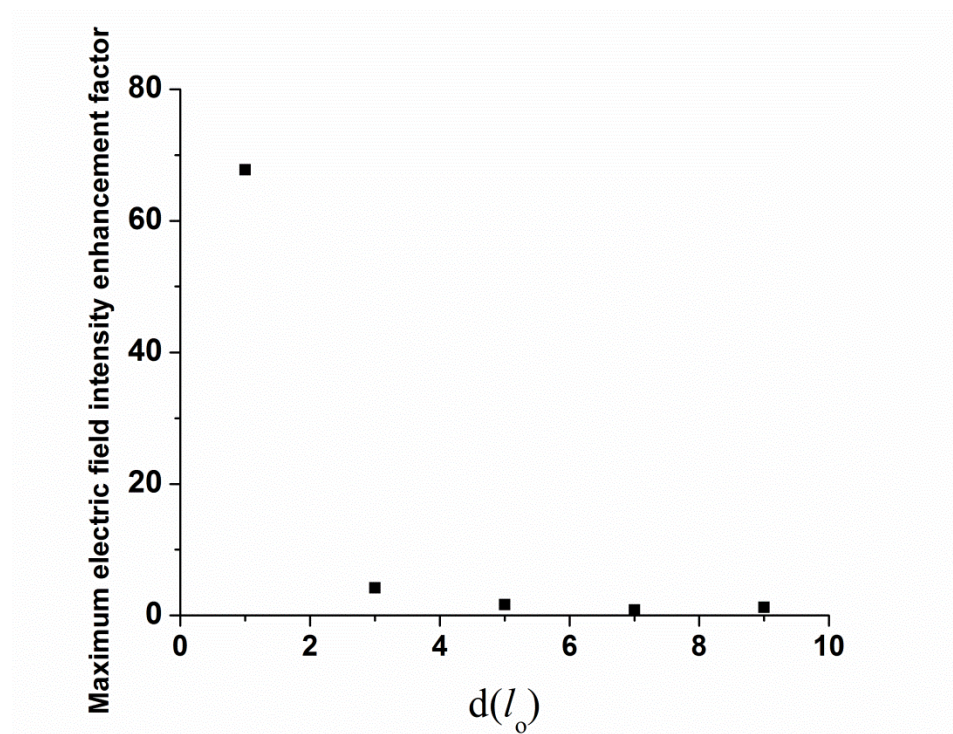


Fig. 4.2 The intensity enhancement factor with different periodicities at $\lambda_0 = 800$ nm.

The electric field intensity enhancement factor of the fractal patterns becomes larger with increasing order of the fractal pattern. Fig. 4.3(a) shows the electric field intensity enhancement factors at different wavelengths, for different types and orders of fractal patterns with $l_0 = 1 \mu\text{m}$ and $P = l_0$. The enhancement factor increases sharply from ~ 7 for $n = 2$ to ~ 70 for $n = 3$, even the geometric change between the two patterns was minimal. When the order of fractal nanostructure becomes higher, the electric field intensity is concentrated near the center of the pattern. In particular, Fig. 4.3(b) shows



the electric field intensity distribution, showing that the electric field intensity is concentrated at the center of the basic unit for $n = 3$. In other words, the electric field intensity is enhanced when the central square of gold is removed. Actually, the motivation of this pattern is to boost the intensity enhancement factor at the center but not at other locations (such as the corners), which has been achieved in the center fractal pattern. Moreover, at an incident wavelength $\lambda = 800$ nm, the maximum intensity enhancement factor of the fractal pattern increases exponentially with increasing order of the fractal pattern nanostructure; in particular, enhancement factors of ~ 5 , ~ 28 , ~ 70 and ~ 127 are achieved for $n = 1, 2, 3$ and 4 respectively (Fig. 4.4). However, the minimum feature sizes for $n = 4$ and $n = 5$ center fractals are 12 nm and 4 nm respectively. Therefore, higher-order center fractal patterns were not studied as the implementation of such features is exceedingly challenging.

The area of edge Au/air interface increases with the order of the fractal structure. Particularly, there is a total Au/air edge interface area of $4 \times l_o/3 \times \text{thickness}$ (33333 nm^2), $(4 \times l_o/3 + 4 \times l_o/9) \times \text{thickness}$ (44444 nm^2) and $(4 \times l_o/3 + 4 \times l_o/9 + 4 \times l_o/27) \times \text{thickness}$ (48148 nm^2) within the basic unit of 1st, 2nd and 3rd order structures, respectively. It should be noted that the thickness of the center fractal structure is 25



nm. Surface plasmons are bounded oscillations of electrons at the interface between a metal and a dielectric [106]. The increasing total area of interface helps to increase the regions for interaction between photons and free electrons of the metal and concentrate the electric field intensity at the center of the nanostructure. As a comparison, the fractal properties in Sierpiński Carpet were also obtained by simulations. In particular, the smallest size of the hole was equal to that in center fractal nanostructure with the same order. For comparison, the electric field intensity distribution for Sierpiński Carpet was also evaluated, and the results are shown in Fig. 4.3(c) [43]. Unlike the center fractal pattern nanostructure, there are a large number of hot spots located at every square hole in the periodic Sierpiński Carpet structure. Fig. 4.3(c) shows the electric field intensity distribution of the Sierpiński Carpet with edge length $l_o = 1\mu\text{m}$ and $n = 3$. The corresponding maximum electric field enhancement factor is ~ 27 at an incident wavelength $\lambda_o = 800\text{ nm}$, which is less than that of the 3rd-order center fractal structure. There are a lot of Au/air interfaces in the Sierpiński Carpet pattern nanostructure and induce a lot of hotspots, but the intensity enhancement factor is lower than that of center fractal pattern nanostructure. Compared with the periodic Sierpiński Carpet pattern, the center fractal pattern can improve electric field intensity enhancement and concentrate



the electric field intensity at the center of the structure.

To prove that the intensity enhancement is in fact due to the center fractal pattern but not the size of the central square, Fig. 4.3(d) shows the electric field distribution of a pattern with only an air square of edge length $l_o/27$ within the square of edge length l_o . The intensity enhancement factor is only ~ 5 , which is much less than that of the 3rd-order center fractal. This proves that the large intensity enhancement is due to the fractal pattern instead of the size of the central square, demonstrating the significance of the fractal in the field enhancement effect.

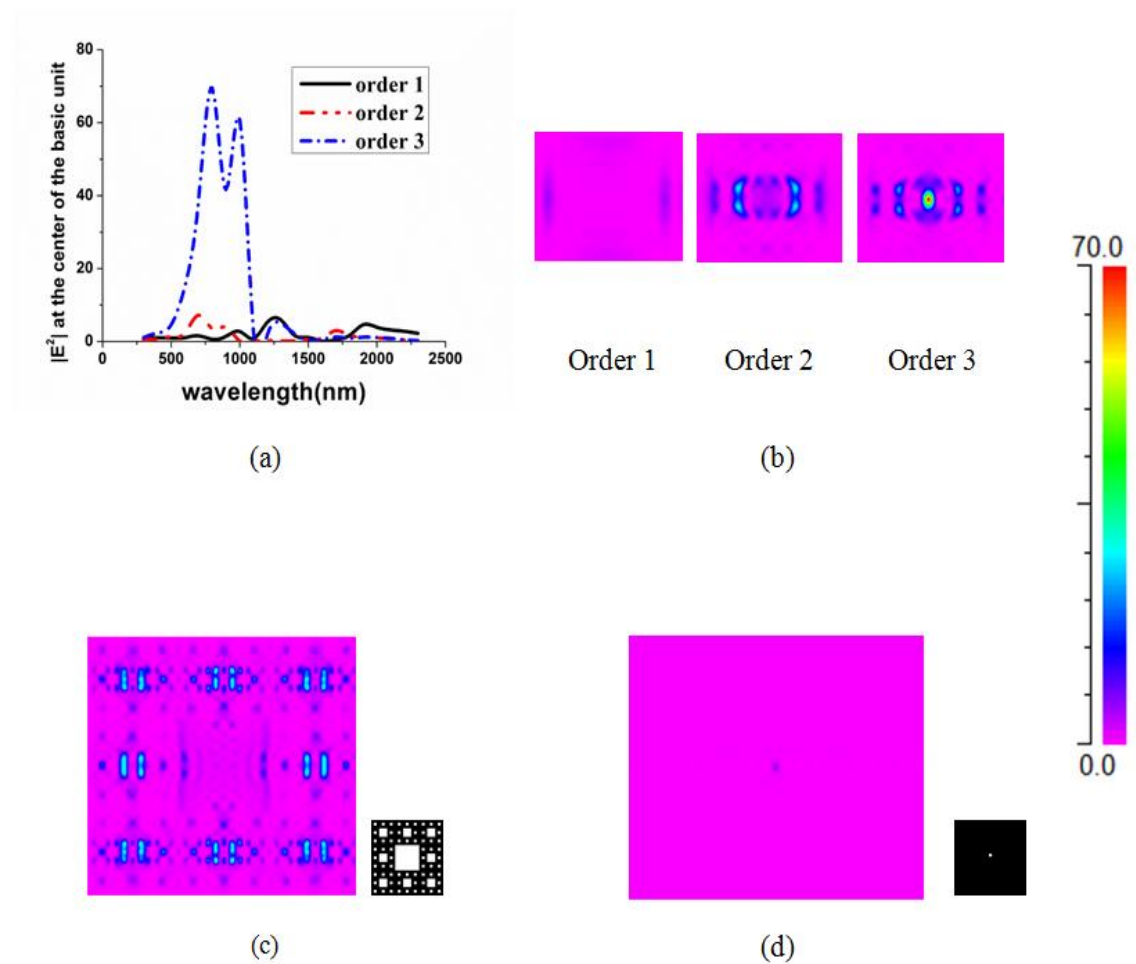


Fig. 4.3 (a) The intensity enhancement at the center of the basic unit of center fractal nanostructure with different orders for $l_o = 1 \mu\text{m}$. (b) Electric field intensity distribution of the center fractal structure with $n = 1, 2, 3$ at $\lambda = 800$ nm. (c) Electric field intensity distribution of the Sierpiński carpet with $n = 3$. (d) Electric field distribution of an air square with length $l_o/27$ at the center of the basic unit in the continuous planar gold film. Small figures next to (c) and (d) indicate the geometric structures of the corresponding Sierpiński carpet and single air hole.

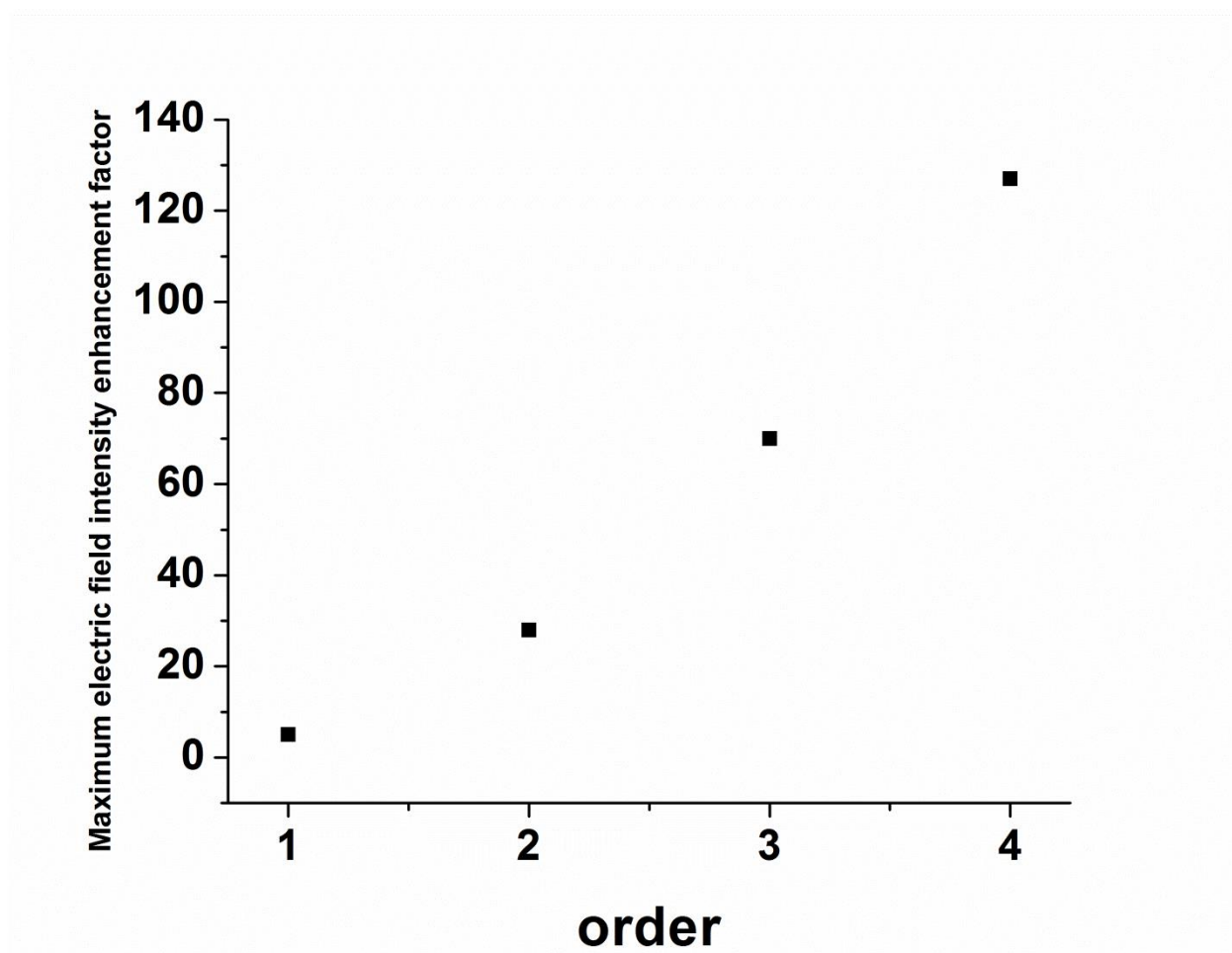


Fig. 4.4 Maximum electric field intensity enhancement factor with different orders of the center fractal.

4.2.3 Influence on transmission spectra and reflection spectra with different structural parameters and compare with Sierpiński Carpet

Compared with gold films without patterns, the center fractal enhances the transmission at the resonant wavelength (transmission peak). Fig. 4.5(a) shows the transmission spectra of the 3rd-order center fractal pattern with different edge lengths l_0 ranging from



500 to 900 nm; the transmission spectrum of planar gold film is also shown for comparison. In case of continuous gold film without patterns, there is only one peak in the transmission spectrum. That transmission peak is due to the electron transition and recombination between the filled d -bands and the Fermi level in the conduction band of the gold film [107-110]. Several resonant peaks (transmission peaks), however, are observed in the periodic fractal pattern structure. Furthermore, simulation results show that the resonant wavelengths can be changed by the basic unit edge length l_o . Fig. 4.5(b) shows the relationship between the resonant wavelengths and edge lengths of basic unit of the center fractal with order $n = 3$ and $P = l_o$. The resonant wavelengths increase linearly with the edge lengths l_o of the basic unit square. This matches the expectation that the resonant wavelength is directly proportional to the size of the aperture. And the transmission peaks depend on periodic condition. The resonant transmission dip matches the matching conditions [39]:

$$\mathbf{k}_o \sin \theta \pm i\mathbf{G}_x \pm j\mathbf{G}_y = \mathbf{k}_{\text{mode}} \quad (4.3)$$

where \mathbf{k}_o is the wave vector of the light incident at a polar angle θ , \mathbf{G}_x and \mathbf{G}_y are the Bragg vectors associated with the two periodicities in x- and y-directions of the array, and i and j are integers indicating the order of the scattering events that couple to the

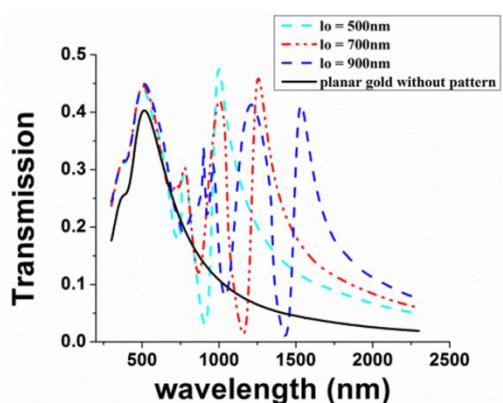


incident light with vector \mathbf{k}_{mode} [39], \mathbf{k}_{mode} is the wave vector of a specific mode of the structure given by:

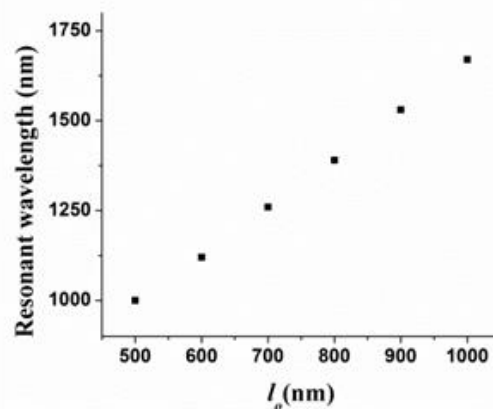
$$\mathbf{k}_{\text{mode}} = \mathbf{k}_0 \sqrt{\frac{\epsilon_m \epsilon_d}{\epsilon_m + \epsilon_d}} \quad (4.4)$$

where ϵ_m and ϵ_d are the dielectric constants of metal and dielectric (nanoimprint resist in this case), respectively.

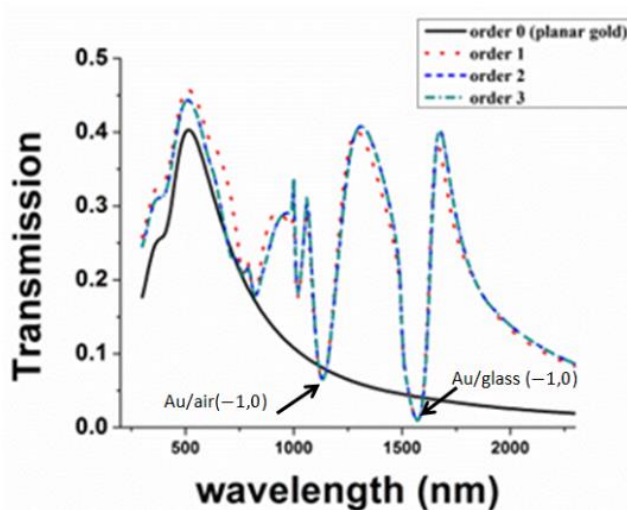
It is found that the transmission spectrum profile is effectively unchanged with increasing order n . Fig. 4.5(c) shows the transmission spectra for centre fractals with $n = 0$ (continuous planar gold film) to $n = 3$ for basic unit with $l_o = 1 \mu\text{m}$ and $P = l_o$. There is a small red shift of $\sim 10 \text{ nm}$ among the whole spectra for $n = 1, 2$ and 3 . Such an effect provides a great advantage in device design, as the desired resonant wavelength can be tuned by the edge length of the basic unit only, while the electric field intensity of the target wavelength can be greatly confined at the center of the basic unit to enhance the light-matter interaction.



(a)



(b)



(c)

Fig. 4.5(a) Transmission spectra of fractal nanostructures with different edge lengths of basic unit for $n = 3$. (b) Relationship between the resonant wavelengths of the third peak of transmission of fractal nanostructures and different edge lengths of basic unit for $n = 3$. (c) Transmission spectra of different orders with edge length $l_0 = 1 \mu\text{m}$ and planer gold film without pattern.



4.3 Summary

I introduced a fractal pattern (center fractal pattern) and investigated its electric field intensity enhancement effect in Au film/glass substrate metal/dielectric system. The effects of three fractal parameters (edge length l_o , periodicity P and order n) on the electric field intensity enhancement factor and transmission spectra were studied numerically. The results showed that the electric field intensity enhancement factor of the periodic center fractal patterns became larger with increasing order of the fractal nanostructures. By calculating the electric field intensity distribution, it was confirmed that the incident electromagnetic wave was confined and enhanced at the center of every basic unit with increasing the order, and the intensity enhancement factor can reach up to 70. Compared with a continuous planar gold film on glass without any pattern, more resonant features were observed in the transmission spectra of the center fractal nanostructure. Under the same period and order, the resonant wavelength increased with the edge length l_o of the basic unit and there was a linear relationship among them.

It is potential for center fractal nanostructure to be used in sensing applications. First, the incident wave is trapped in the center of every basic unit in center fractal. This local



electric field enhancement is of particular interest as it increases the effective intensity of the incident electromagnetic wave and leads to some phenomena such as surface enhanced Raman scattering (SERS) [111, 112], improve efficiency of various nonlinear process [113-116] and surface enhanced fluorescence [117].



Chapter 5

Thermally-tunable plasmonic resonance based on ferroelectric polymer P(VDF-TrFE)

5.1 Introduction

Thermal tuning is one of the schemes for modulating surface plasmon resonance (SPR) modes, which is relatively easy to implement and control. Thermally-modulated SPR has been reported in metal nano-particles placed on top dielectric surfaces and in nano-composites formed by embedding the metal nano-particles inside the dielectric [49, 118]. On the other hand, one and two-dimensional periodic structures were also used because it is able to control the geometric parameters such as periodicity, edge length and feature depth, in order to optimize the SPR. However, there is a lack of experimental and numerical investigations for thermal tuning of SPR in one- or two-dimensional metal/dielectric nanostructures [119].

VO₂ is very commonly investigated in thermal tuning of SPR because it demonstrates a large variation of refractive index (~2.8 to ~2.2) from room temperature to 80°C at 600 nm, which is induced by the metal-insulator phase transition around 65°C [49, 50, 120].

Barium-strontium titanate (Ba_{0.7}Sr_{0.3})TiO₃ (BST) thin films have also been used in SPR



thermal tuning investigation, as the refractive index of BST thin films can be changed from 2.3932 (TE)/1.9945 (TM) at room temperature to 2.3949 (TE)/1.9965 (TM) at 66°C [52].

Poly-vinylidene fluoride (PVDF) was the first identified ferroelectric polymer. PVDF shows no Curie temperature, as melting occurs at a lower temperature than the phase transition [56]. Usually, PVDF crystallizes into a non-ferroelectric crystal phase and must be converted to ferroelectric phase by stretching or high electric-field poling [121, 122]. The incorporation of trifluoroethylene (TrFE) into PVDF greatly facilitates the formation of the ferroelectric phase [121]. The phase transition behavior of PVDF strongly depends on the thermal history of the material [56], And it is simple for patterning to realize thermal tuning. Hence, poly[(vinylidene fluoride-co-trifluoroethylene) P(VDF-TrFE) was chosen as the dielectric material in one dimensional (1D) grating nanostructure in this project to develop active plasmonic devices. The 1D gratings were fabricated on P(VDF-TrFE) surfaces by nano-imprint lithography; such a technique is scalable for large-area patterning. The thermal tuning of SPR was characterized by refractive index measurement and the reflectivity calculation, based on the Rigorous Coupled Wave Analysis (RCWA) simulations. The results



indicate the feasibility of active modulation in SPR in solid-state nanostructures.

5.2 Fabrication of plasmonic structure based on ferroelectric polymer P(VDF-TrFE)

Nanoimprint lithography was employed in this work and the procedures are summarized in Fig. 5.1. The mole ratio of VDF and TrFE in the copolymer was kept at 70 to 30. A P(VDF-TrFE) copolymer layer of thickness 200 nm was spin-coated on the silicon substrate. A polydimethylsiloxane (PDMS) mold containing a grating pattern (period 750 nm, width 375 nm) was then pressed against a 100-150 kPa-pressure at 180°C for 10 minutes, that the grating pattern was transferred onto the P(VDF-TrFE) layer. The imprinted layer of P(VDF-TrFE) was annealed at 120°C for 2 hours. 25 nm of Au was then deposited by sputtering. In order to reduce the plasmonic effect between Au and air that would interfere with the results interpretation, a P(VDF-TrFE) layer of thickness 230 nm was spin-coated on the gold surface to ensure that there were only Au/P(VDF-TrFE) interfaces in the structure. Finally, the sample was annealed at 120°C for 2 hours again. Fig. 5.2 shows that the depth of grating was around 140 nm, as measured by atomic force microscope (AFM).

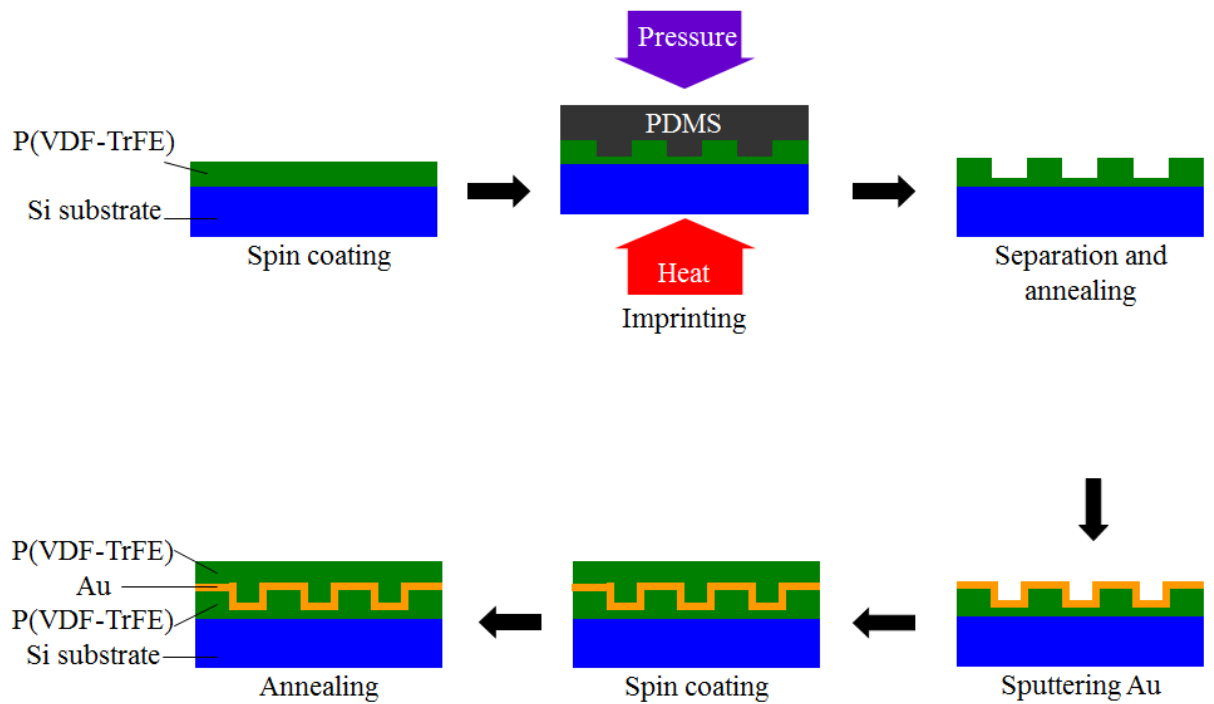


Fig. 5.1 Schematic of process flow for fabrication of Au/P(VDF-TrFE) grating structure.

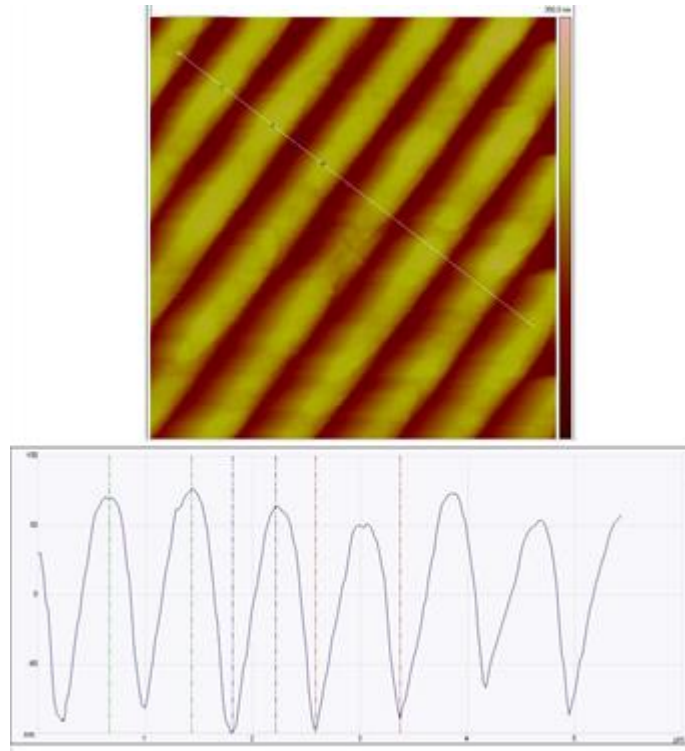


Fig. 5.2 AFM image (upper panel) and sectional profile (lower panel) of the grating pattern after nanoimprint lithography. The depth of the grating was about 140nm.

5.3 Characterization of plasmonic structure based on ferroelectric polymer P(VDF-TrFE)

5.3.1 Optical characterization of ferroelectric polymer P(VDF-TrFE)

The refractive indices of P(VDF-TrFE) at different temperatures were measured by ellipsometry performed at different wavelengths, and the results are shown in Fig. 5.3.

At a wavelength of 633 nm, the refractive index reduces from 1.4009 to 1.3521 as the temperature changes from 30°C to 130°C. Significantly, a thermal hysteresis behavior is



observed.

The temperature dependence of the linear and nonlinear dielectric functions of ferroelectric crystallites can be phenomenologically described by the Landau theory of phase transition. Within the framework of the Landau theory, the free energy F of a ferroelectric crystallite is given by [123]

$$F = F_0 + \frac{1}{2}\alpha D^2 + \frac{1}{4}\gamma D^4 + \frac{1}{6}\delta D^6 \quad (5.1)$$

with the Landau parameters α , γ and δ and electric displacement field D .

The coefficients ε_n , n is positive integer, of the dielectric displacement in terms of the electric field E in the power series representation is written as:

$$D = P_0 + \varepsilon_0 \varepsilon_1 E + \varepsilon_0 \varepsilon_2 E^2 + \varepsilon_0 \varepsilon_3 E^3 + \dots \quad (5.2)$$

In the ferroelectric phase, the second-order permittivity depends on the remanent polarization P_r and the spontaneous polarization P_s [124]:

$$\varepsilon_0 \varepsilon_2 = -P_r (\varepsilon_0 \varepsilon_1)^3 (3\gamma + 10\delta P_s^2) \quad (5.3)$$

The temperature dependence of $1/\varepsilon_1$ in the ferroelectric phase gives a criterion: if $10\delta P_s^2$ is small compared to 3γ , then $\varepsilon_2 / \varepsilon_1^3$ is proportional to the remanent polarization:



$$\frac{\epsilon_0 \epsilon_2}{3(\epsilon_0 \epsilon_1)^3} = -P_r \quad (5.4)$$

For P(VDF-TrFE) copolymer of molar ratio 70/30, the phase transition is of first order, as is evident from the thermal hysteresis upon heating and cooling. B. Heiler *et al.* claimed there was no thermal hysteresis in 56/44 copolymer blend [125].

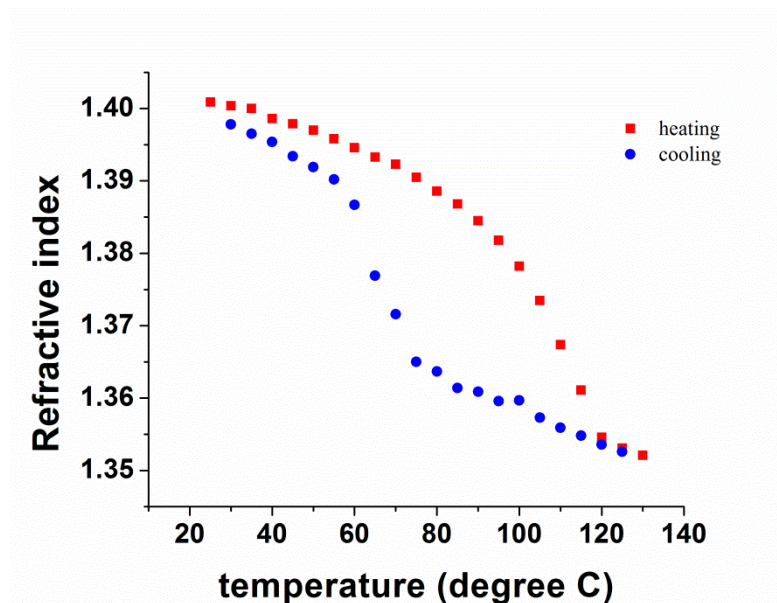


Fig. 5.3 Temperature dependence of refractive index of P(VDF-TrFE) at 633 nm incident wavelength, as measured by ellipsometry.

5.3.2 Computational study of surface plasmon resonance of ferroelectric polymer

P(VDF-TrFE)

5.3.2.1 Simulation model

The simulated reflection spectra were obtained by DiffractMod of RSoft™. The side



view of the simulated nanostructure is shown in Fig. 5.4. The thickness of the ferroelectric copolymer was 200 nm. The depth and width of the grating structure were 110 and 375 nm respectively, with a periodicity of 750 nm. The thickness of the Au layer was kept at 25 nm, and the Si substrate was regarded as semi-infinite layer in the analysis. Transverse-magnetic (TM) polarized light was considered in this investigation. The incident wave was launched from air. The refractive indices of P(VDF-TrFE) were obtained by ellipsometry measurements. The material database of DiffractMod of RSoft™ [66] was adopted for the simulation of dielectric properties of Au and Si, based on the combined Drude and multiple Lorentzian models [33]:

$$\varepsilon_r(\omega) = 1 - \omega_p^2 / \omega^2 \quad (5.5)$$

where ε_r is dielectric constant, ω_p is the plasma frequency of gold in the free electron model.

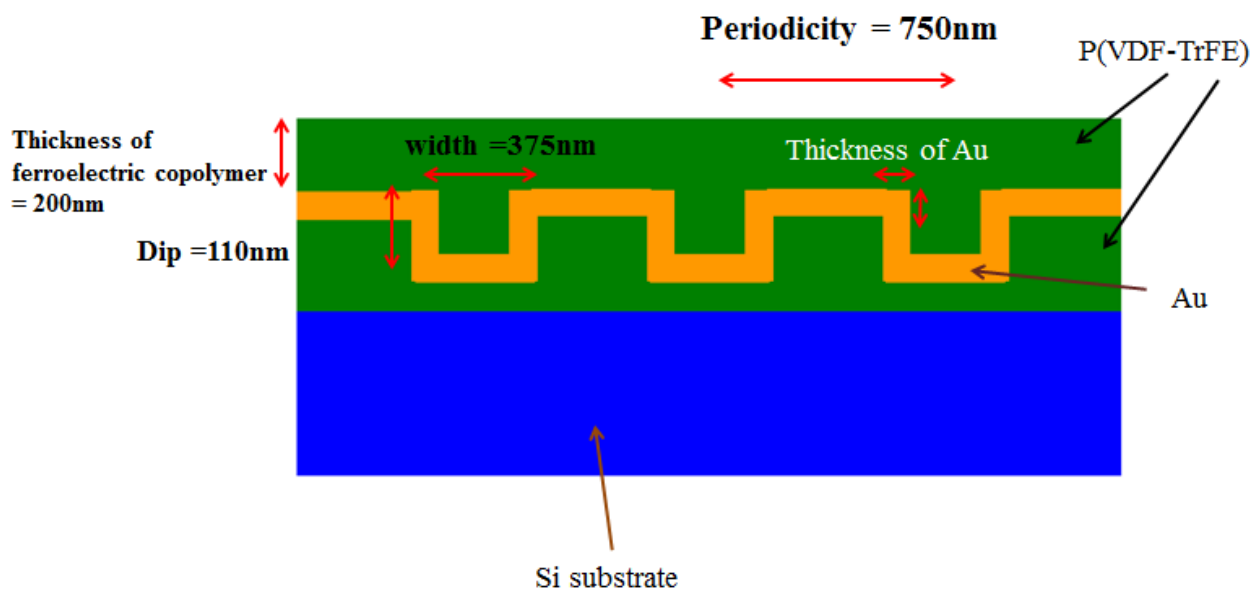


Fig. 5.4 Schematic of the simulation model.

5.3.2.2 Surface plasmon resonance of ferroelectric polymer

Reflectivity as a function of temperature was used to investigate the plasmonic properties of the samples. Fig. 5.5 shows the simulated reflection spectra at 30°C, 80°C and 130°C of the structure, in both the heating and cooling parts of the cycle. The incident angle of the electromagnetic wave was fixed at 20°. The reflection dip is due to the coupling between incident wave and surface plasmon modes [39]. The dip positions depend on the temperature, and the resonance wavelengths are blue-shifted and red-shifted during the heating and cooling process, respectively. The shifting is ~16 nm in heating process.



On the other hand, Fig. 5.6 shows the measured reflection spectra at 30°C (RT) and 130°C (HT) with an incident angle of 20° for the light. The simulation results match the measurement results. Two results both show that the shifting of resonant wavelength is up to ~16 nm between 30°C to 130°C. Also, Fig. 5.7 shows the simulated reflection spectrum based on the measurement of refractive index with different temperatures. The hysteresis loop also appears between resonant wavelengths and temperatures. The change in resonant wavelength is due to the ferroelectric properties that were discussed in the previous section. Similar to the hysteresis loop of refractive indices, the largest difference between heating and cooling is at 80°C. This shows that the position of SPR depends on thermal history; the position of SPR of the structure can be tuned by external temperature.

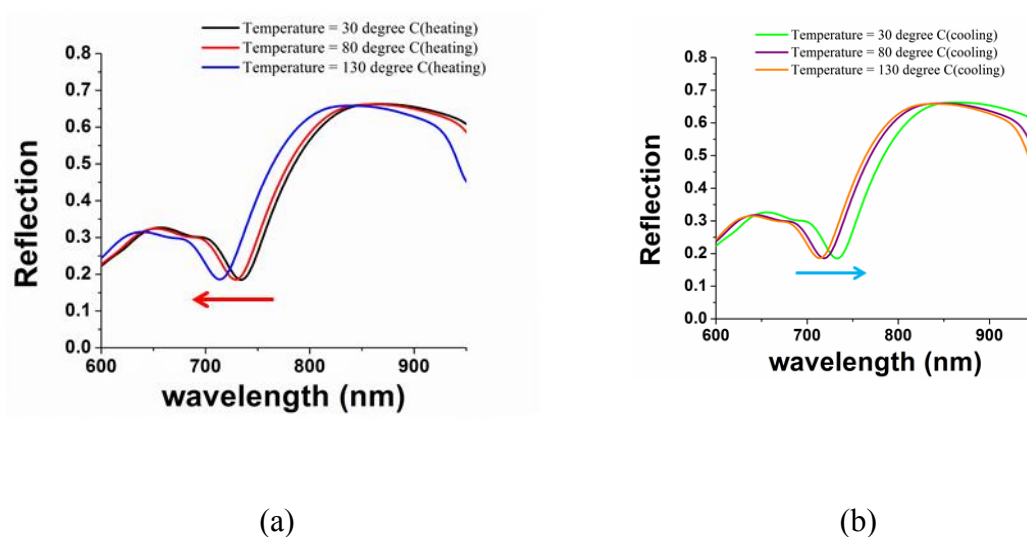


Fig. 5.5 Simulated reflection spectra of 30, 80 and 130°C in (a) heating and (b) cooling at 20° incident angle.

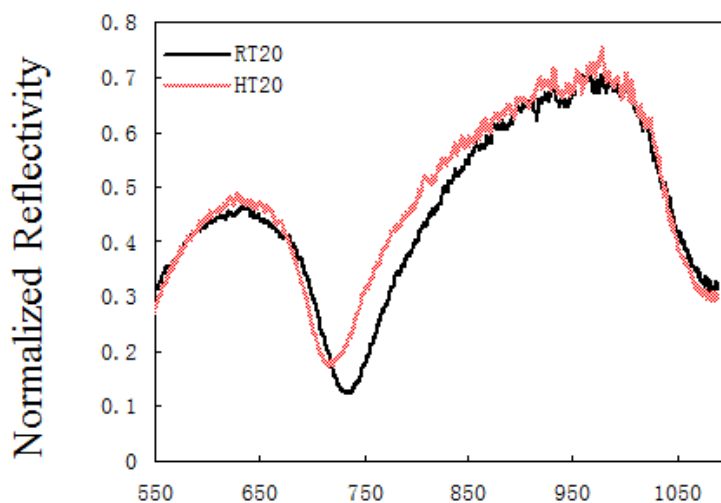


Fig. 5.6 Measured reflection spectra of 30°C and 130°C at 20° incident angle.

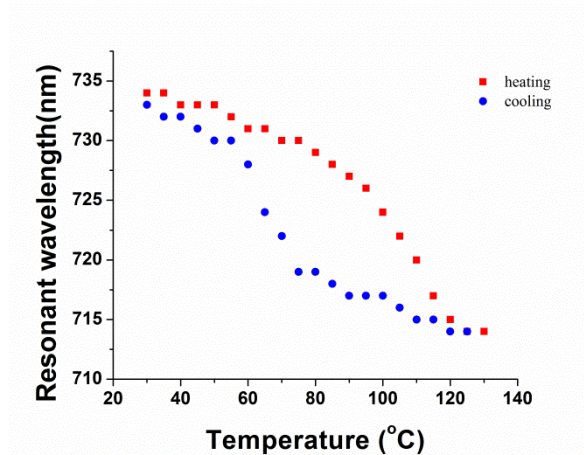


Fig. 5.7 Calculated resonant wavelengths in heating and cooling at 20° incidence angle.

5.4 Summary

A periodic ferroelectric copolymer grating nanostructure with a period of 750 nm was investigated. A maximum refractive index shift of ~ 0.0488 was observed, when the sample temperature increased from 30°C to 130°C. A hysteretic behavior of the refractive index in the copolymer was observed upon heating and cooling. Simulations based on measured refractive indices show that the shifting of SPR wavelength was up to ~ 16 nm, which was significant as compared with previous studies [52]. The change in refractive index and resonant reflection dip position depends on the thermal history of the sample. Due to the large shifting, the sensitivity in thermal sensing based on ferroelectric polymer P(VDF-TrFE) is enhanced.



Chapter 6

Conclusions

The present research focused on the optical properties of three types of periodic plasmonic structures, which were investigated by simulation using the Rigorous Coupled Wave Analysis (RCWA) method and experiments.

First of all, a periodic plasmonic nano-pillar structure was investigated in the interaction between the top gold cap and perforated gold film. These interaction between the two systems induced CSPR. In CSPR, the incident wave was confined at the surrounding of the nano-pillars. The resonant wavelength of CSPR reduced with the height of the nano-pillar exponentially. The dip positions of PSRPs were independent of the height of nano-pillars but were dependent on the incident angle. In contrast, the dip positions of CSPR were dependent on the height of nano-pillars but were independent of the incident angle. The electric field intensity enhancement in CSPR became weaker with increasing height of nano-pillars. Lastly, the periodic plasmonic nano-pillar structure can be used in for refractive index sensing.

Secondly, a fractal pattern (center fractal pattern) was investigated in its electric field intensity enhancement effect in Au film/glass substrate metal/dielectric system. The



effects of three structural parameters (edge length l_o , periodicity P and order n) on the electric field intensity enhancement and transmission spectra were studied numerically.

The results showed that the electric field intensity enhancement factor of the periodic center fractal patterns became larger with increasing order of the fractal nanostructures.

By calculating the electric field intensity distribution, it was confirmed that the incident electromagnetic wave was confined and enhanced at the center of every basic unit with increasing order, and the intensity enhancement factor can reach up to 70. Compared with a continuous planar gold film on glass without any pattern, more resonant features were observed in the transmission spectra of the fractal nanostructure. Under the same period and order, the resonant wavelength increased with the edge length l_o of the basic unit, and there was a linear relationship among them.

Finally, a periodic ferroelectric copolymer grating nanostructure with a period of 750 nm was investigated. A maximum refractive index shift of ~ 0.0488 was observed, when the sample temperature increased from 30°C to 130°C . A hysteretic behavior of the refractive index in the copolymer was observed upon heating and cooling. Simulations based on measured refractive index showed that the shifting of SPR wavelength was up to ~ 16 nm. The change in refractive index and resonant reflection dip position depended



on the thermal history of the sample. Due to the large shifting, the sensitivity in thermal sensing based on ferroelectric polymer P(VDF-TrFE) is also enhanced.

**References**

- [1] Z. Junxi, Z. Lide, and X. Wei, "Surface plasmon polaritons: physics and applications," *Journal of Physics D: Applied Physics*, vol. 45, pp. 113001, 2012.
- [2] R. W. Wood, "XLII. On a remarkable case of uneven distribution of light in a diffraction grating spectrum," *Philosophical Magazine Series 6*, vol. 4, pp. 396-402, 1902.
- [3] J. C. M. Garnett, "Colours in Metal Glasses and in Metallic Films," *Philosophical Transactions of the Royal Society of London. Series A, Containing Papers of a Mathematical or Physical Character*, vol. 203, pp. 385-420, 1904.
- [4] G. Mie, "Beiträge zur Optik trüber Medien, speziell kolloidaler Metallösungen," *Annalen der Physik*, vol. 330, pp. 377-445, 1908.
- [5] D. Pines, "Collective Energy Losses in Solids," *Reviews of Modern Physics*, vol. 28, pp. 184-198, 1956.
- [6] U. Fano, "Atomic Theory of Electromagnetic Interactions in Dense Materials," *Physical Review*, vol. 103, pp. 1202-1218, 1956.
- [7] R. H. Ritchie, "Plasma Losses by Fast Electrons in Thin Films," *Physical Review*, vol. 106, pp. 874-881, 1957.
- [8] R. H. Ritchie, E. T. Arakawa, J. J. Cowan, and R. N. Hamm, "Surface-Plasmon Resonance Effect in Grating Diffraction," *Physical Review Letters*, vol. 21, pp. 1530-1533, 1968.
- [9] A. Otto, "Excitation of nonradiative surface plasma waves in silver by the method of frustrated total reflection," *Zeitschrift für Physik*, vol. 216, pp. 398-410, 1968.
- [10] M. Quinten, A. Leitner, J. R. Krenn, and F. R. Aussenegg, "Electromagnetic energy transport via linear chains of silver nanoparticles," *Optics Letters*, vol. 23, pp. 1331-1333, 1998.
- [11] S. A. Maier, P. G. Kik, H. A. Atwater, S. Meltzer, E. Harel, B. E. Koel, *et al.*, "Local detection of electromagnetic energy transport below the diffraction limit in metal nanoparticle plasmon waveguides," *Nature Materials*, vol. 2, pp. 229-232, 2003.



- [12] J.-C. Weeber, A. Dereux, C. Girard, J. R. Krenn, and J.-P. Goudonnet, "Plasmon polaritons of metallic nanowires for controlling submicron propagation of light," *Physical Review B*, vol. 60, pp. 9061-9068, 1999.
- [13] S. I. Bozhevolnyi, J. Erland, K. Leosson, P. M. W. Skovgaard, and J. M. Hvam, "Waveguiding in Surface Plasmon Polariton Band Gap Structures," *Physical Review Letters*, vol. 86, pp. 3008-3011, 2001.
- [14] S. I. Bozhevolnyi, V. S. Volkov, E. Devaux, and T. W. Ebbesen, "Channel Plasmon-Polariton Guiding by Subwavelength Metal Grooves," *Physical Review Letters*, vol. 95, p. 046802, 2005.
- [15] S. I. Bozhevolnyi, V. S. Volkov, E. Devaux, J.-Y. Laluet, and T. W. Ebbesen, "Channel plasmon subwavelength waveguide components including interferometers and ring resonators," *Nature*, vol. 440, pp. 508-511, 2006.
- [16] R. F. Oulton, V. J. Sorger, D. A. Genov, D. F. P. Pile, and X. Zhang, "A hybrid plasmonic waveguide for subwavelength confinement and long-range propagation," *Nature Photonics*, vol. 2, pp. 496-500, 2008.
- [17] P. Nagpal, N. C. Lindquist, S.H. Oh, and D. J. Norris, "Ultrasoother Patterned Metals for Plasmonics and Metamaterials," *Science*, vol. 325, pp. 594-597, 2009.
- [18] O. Stenzel, A. Stendal, K. Voigtsberger, and C. von Borczyskowski, "Enhancement of the photovoltaic conversion efficiency of copper phthalocyanine thin film devices by incorporation of metal clusters," *Solar Energy Materials and Solar Cells*, vol. 37, pp. 337-348, 1995.
- [19] M. Westphalen, U. Kreibig, J. Rostalski, H. Lüth, and D. Meissner, "Metal cluster enhanced organic solar cells," *Solar Energy Materials and Solar Cells*, vol. 61, pp. 97-105, 2000.
- [20] V. E. Ferry, L. A. Sweatlock, D. Pacifici, and H. A. Atwater, "Plasmonic Nanostructure Design for Efficient Light Coupling into Solar Cells," *Nano Letters*, vol. 8, pp. 4391-4397, 2008.
- [21] M. D. Brown, T. Suteewong, R. S. S. Kumar, V. D'Innocenzo, A. Petrozza, M. M. Lee, *et al.*, "Plasmonic Dye-Sensitized Solar Cells Using Core-Shell Metal-Insulator Nanoparticles," *Nano Letters*, vol. 11, pp. 438-445, 2010.
- [22] G. Raschke, S. Brogl, A. S. Susha, A. L. Rogach, T. A. Klar, J. Feldmann, *et al.*, "Gold Nanoshells Improve Single Nanoparticle Molecular Sensors," *Nano Letters*, vol. 4, pp. 1853-1857, 2004.



- [23] M.-C. Daniel and D. Astruc, "Gold Nanoparticles: Assembly, Supramolecular Chemistry, Quantum-Size-Related Properties, and Applications toward Biology, Catalysis, and Nanotechnology," *Chemical Reviews*, vol. 104, pp. 293-346, 2003.
- [24] F. Goettmann, A. Moores, C. Boissière, P. Le Floch, and C. Sanchez, "A Selective Chemical Sensor Based on the Plasmonic Response of Phosphinine-Stabilized Gold Nanoparticles Hosted on Periodically Organized Mesoporous Silica Thin Layers," *Small*, vol. 1, pp. 636-639, 2005.
- [25] G. Nemova and R. Kashyap, "Theoretical model of a planar waveguide refractive index sensor assisted by a corrugated long period metal grating," *Optics Communications*, vol. 281, pp. 1522-1528, 2008.
- [26] G. Nemova and R. Kashyap, "Fiber-Bragg-grating-assisted surface plasmon-polariton sensor," *Optics Letters*, vol. 31, pp. 2118-2120, 2006.
- [27] G. Nemova and R. Kashyap, "Theoretical model of a planar integrated refractive index sensor based on surface plasmon-polariton excitation," *Optics Communications*, vol. 275, pp. 76-82, 2007.
- [28] S. M. Tripathi, A. Kumar, E. Marin, and J. P. Meunier, "Side-Polished Optical Fiber Grating-Based Refractive Index Sensors Utilizing the Pure Surface Plasmon Polariton," *Journal of Lightwave Technology*, vol. 26, pp. 1980-1985, 2008.
- [29] J. N. Anker, W. P. Hall, O. Lyandres, N. C. Shah, J. Zhao, and R. P. Van Duyne, "Biosensing with plasmonic nanosensors," *Nature Materials*, vol. 7, pp. 442-453, 06/print 2008.
- [30] N. L. Rosi and C. A. Mirkin, "Nanostructures in Biodiagnostics," *Chemical Reviews*, vol. 105, pp. 1547-1562, 2005.
- [31] M. S. Han, A. K. R. Lytton-Jean, B.K. Oh, J. Heo, and C. A. Mirkin, "Colorimetric Screening of DNA-Binding Molecules with Gold Nanoparticle Probes," *Angewandte Chemie International Edition*, vol. 45, pp. 1807-1810, 2006.
- [32] A. V. Kabashin, P. Evans, S. Pastkovsky, W. Hendren, G. A. Wurtz, R. Atkinson, *et al.*, "Plasmonic nanorod metamaterials for biosensing," *Nature Materials* vol. 8, pp. 867-871, 2009.
- [33] M. Fox, *Optical properties of solids*. Oxford: Oxford University Press, 2001.



- [34] M. Born and E. Wolf, *Principles of optics : electromagnetic theory of propagation, interference and diffraction of light*, 6th (corr.) ed. Cambridge, New York, N.Y.: Cambridge University Press, 1997.
- [35] D. J. Griffiths, *Introduction to electrodynamics*, 3rd ed. Upper Saddle River, N.J. Prentice Hall, 1999.
- [36] *Optical properties of solids*. Oxford: Oxford University Press, 2001.
- [37] G. Popescu, *Nanobiophotonics*. New York: McGraw-Hill, 2010.
- [38] H. Raether, *Surface plasmons on smooth and rough surfaces and on gratings*: Springer, 1988.
- [39] W. L. Barnes, W. A. Murray, J. Dintinger, E. Devaux, and T. W. Ebbesen, "Surface Plasmon Polaritons and Their Role in the Enhanced Transmission of Light through Periodic Arrays of Subwavelength Holes in a Metal Film," *Physical Review Letters*, vol. 92, p. 107401, 2004.
- [40] X. Huang, S. Xiao, D. Ye, J. Huangfu, Z. Wang, L. Ran, *et al.*, "Fractal plasmonic metamaterials for subwavelength imaging," *Optics Express*, vol. 18, pp. 10377-10387, 2010.
- [41] D. H. Werner and S. Ganguly, "An overview of fractal antenna engineering research," *IEEE Antennas and Propagation Magazine*, vol. 45, pp. 38-57, 2003.
- [42] G. Volpe, G. Volpe, and R. Quidant, "Fractal plasmonics: subdiffraction focusing and broadband spectral response by a Sierpinski nanocarpet," *Optics Express*, vol. 19, pp. 3612-3618, 2011.
- [43] J. Feder, *Fractals*. New York: Plenum Press, 1988.
- [44] S. Sederberg and A. Y. Elezzabi, "Sierpinski carpet fractal plasmonic antenna: a fractal abstraction of the plasmonic bowtie antenna," *Optics Express*, vol. 19, pp. 10456-10461, 2011.
- [45] J. Anguera, C. Puente, C. Borja, R. Montero, and J. Soler, "Small and high-directivity bow-tie patch antenna based on the Sierpinski fractal," *Microwave and Optical Technology Letters*, vol. 31, pp. 239-241, 2001.
- [46] D. L. Jaggard and T. Spielman, "Triadic cantor target diffraction," *Microwave and Optical Technology Letters*, vol. 5, pp. 460-466, 1992.
- [47] C. Puente-Baliarda, J. Romeu, R. Pous, and A. Cardama, "On the behavior of the Sierpinski multiband fractal antenna," *IEEE Transactions on Antennas and Propagation*, vol. 46, pp. 517-524, 1998.



- [48] J. Matteo and L. Hesselink, "Fractal extensions of near-field aperture shapes for enhanced transmission and resolution," *Optics Express*, vol. 13, pp. 636-647, 2005.
- [49] J. Y. Suh, E. U. Donev, D. W. Ferrara, K. A. Tetz, L. C. Feldman, and J. R. F. Haglund, "Modulation of the gold particle-plasmon resonance by the metal-semiconductor transition of vanadium dioxide," *Journal of Optics A: Pure and Applied Optics*, vol. 10, p. 055202, 2008.
- [50] J. Y. Suh, E. U. Donev, R. Lopez, L. C. Feldman, and R. F. Haglund, "Modulated optical transmission of subwavelength hole arrays in metal-VO₂ films," *Applied Physics Letters*, vol. 88, 2006.
- [51] H. Buhay, K. J. Kogler, B. L. Whitehead, and R. C. Tiberio, "Summary Abstract: Reactive ion etching of vanadium dioxide thin films," *Journal of Vacuum Science & Technology A: Vacuum, Surfaces, and Films*, vol. 4, pp. 440-442, 1986.
- [52] J. Z. Xin, K. C. Hui, K. Wang, H. L. W. Chan, D. H. C. Ong, and C. W. Leung, "Thermal tuning of surface plasmon resonance: Ag gratings on barium strontium titanate thin films," *Applied Physics A*, vol. 107, pp. 101-107, 2012.
- [53] D.-Y. Wang, H. L. W. Chan, and C. L. Choy, "Fabrication and characterization of epitaxial Ba_{0.7}Sr_{0.3}TiO₃ thin films for optical waveguide applications," *Applied Optics*, vol. 45, pp. 1972-1978, 2006.
- [54] D. Y. Wang, J. Wang, H. L. W. Chan, and C. L. Choy, "Structural and electro-optic properties of Ba_{0.7}Sr_{0.3}TiO₃ thin films grown on various substrates using pulsed laser deposition," *Journal of Applied Physics*, vol. 101, 2007.
- [55] K. L. Jim, D. Y. Wang, C. W. Leung, C. L. Choy, and H. L. W. Chan, "One-dimensional tunable ferroelectric photonic crystals based on Ba_{0.7}Sr_{0.3}TiO₃/MgO multilayer thin films," *Journal of Applied Physics*, vol. 103, 2008.
- [56] S. Bauer, "Poled polymers for sensors and photonic applications," *Journal of Applied Physics*, vol. 80, pp. 5531-5558, 1996.
- [57] D. C. Bassett, *Developments in Crystalline Polymers: Applied Science Publishers*, 1982.
- [58] B. Ploss and B. Ploss, "Dielectric nonlinearity of PVDF-TrFE copolymer," *Polymer*, vol. 41, pp. 6087-6093, 2000.



- [59] J. Homola, S. S. Yee, and G. Gauglitz, "Surface plasmon resonance sensors: review," *Sensors and Actuators B: Chemical*, vol. 54, pp. 3-15, 1999.
- [60] D. Sarid, "Long-Range Surface-Plasma Waves on Very Thin Metal Films," *Physical Review Letters*, vol. 47, pp. 1927-1930, 1981.
- [61] P. Berini, "Long-range surface plasmon polaritons," *Advances in Optics and Photonics*, vol. 1, pp. 484-588, 2009.
- [62] Y. Shen, J. Zhou, T. Liu, Y. Tao, R. Jiang, M. Liu, *et al.*, "Plasmonic gold mushroom arrays with refractive index sensing figures of merit approaching the theoretical limit," *Nature Communications*, vol. 4, 2013.
- [63] R. Petit and L. C. Botten, *Electromagnetic theory of gratings*: Springer-Verlag, 1980.
- [64] M. G. Moharam and T. K. Gaylord, "Rigorous coupled-wave analysis of metallic surface-relief gratings," *Journal of the Optical Society of America A*, vol. 3, pp. 1780-1787, 1986.
- [65] L. Li, "New formulation of the Fourier modal method for crossed surface-relief gratings," *Journal of the Optical Society of America A*, vol. 14, pp. 2758-2767, 1997.
- [66] R. D. Group, "DiffractMOD User Guide".
- [67] W. M. Choi and O. O. Park, "A soft-imprint technique for submicron-scale patterns using a PDMS mold," *Microelectronic Engineering*, vol. 73-74, pp. 178-183, 2004.
- [68] K. L. Jim, F. K. Lee, J. Z. Xin, C. W. Leung, H. L. W. Chan, and Y. Chen, "Fabrication of nano-scaled patterns on ceramic thin films and silicon substrates by soft ultraviolet nanoimprint lithography," *Microelectronic Engineering*, vol. 87, pp. 959-962, 2010.
- [69] G. Barbillon, F. Hamouda, S. Held, P. Gogol, and B. Bartenlian, "Gold nanoparticles by soft UV nanoimprint lithography coupled to a lift-off process for plasmonic sensing of antibodies," *Microelectronic Engineering*, vol. 87, pp. 1001-1004, 2010.
- [70] A. Montaser and D. W. Golightly, *Inductively coupled plasmas in analytical atomic spectrometry*. Weinheim: Weinheim : VCH Verlags Gesellschaft, c1987., 1987.



- [71] X. Jianzhuo, "Tunable photonic devices in ferroelectric-based layered structures," PhD, Applied Physics in The Hong Kong Polytechnic University, 2012.
- [72] *Physical vapor deposition of thin films*. New York: Wiley, 2000.
- [73] *Principles of physical vapor deposition of thin films*, 1st ed. Amsterdam Boston London: Elsevier, 2006.
- [74] L. Reimer, *Scanning Electron Microscopy: Physics of Image Formation and Microanalysis*: Springer, 1998.
- [75] D. A. Bonnell, *Scanning probe microscopy and spectroscopy : theory, techniques, and applications*, 2nd ed. New York: Wiley, 2001.
- [76] F. J. Owens, *Introduction to nanotechnology*. Hoboken, NJ: John Wiley, 2003.
- [77] C. Y. Chan, J. B. Xu, M. Y. Waye, and H. C. Ong, "Angle resolved surface enhanced Raman scattering (SERS) on two-dimensional metallic arrays with different hole sizes," *Applied Physics Letters*, vol. 96, 2010.
- [78] J. Li, "Experimental and theoretical studies of the optical properties of periodic metallic nanostructures" Ph. D, The Chinese University of Hong Kong, 2009.
- [79] L. Novotny, B. Hecht, and I. ebrary, "Principles of nano-optics," 2nd ed. Cambridge: Cambridge University Press, 2012.
- [80] D. Sarid and W. A. Challener, *Modern introduction to surface plasmons : theory, Mathematica modeling, and applications*. Cambridge, New York: Cambridge University Press, 2010.
- [81] S. A. Maier, "Plasmonics fundamentals and applications," ed. New York: Springer, 2007.
- [82] H. Raether, *Surface Plasmons on Smooth and Rough Surfaces and on Gratings*: Springer, 1988.
- [83] C. R. Yonzon, E. Jeoung, S. Zou, G. C. Schatz, M. Mrksich, and R. P. Van Duyne, "A Comparative Analysis of Localized and Propagating Surface Plasmon Resonance Sensors: The Binding of Concanavalin A to a Monosaccharide Functionalized Self-Assembled Monolayer," *Journal of the American Chemical Society*, vol. 126, pp. 12669-12676, 2004.
- [84] K. M. Mayer and J. H. Hafner, "Localized Surface Plasmon Resonance Sensors," *Chemical Reviews*, vol. 111, pp. 3828-3857, 2011.



- [85] N. A. Hatab, C.-H. Hsueh, A. L. Gaddis, S. T. Retterer, J.-H. Li, G. Eres, *et al.*, "Free-Standing Optical Gold Bowtie Nanoantenna with Variable Gap Size for Enhanced Raman Spectroscopy," *Nano Letters*, vol. 10, pp. 4952-4955, 2010.
- [86] R. D. G. Inc, "DiffractMOD User Guide," ed. New York, USA, 2012.
- [87] M. Fox, *Optical properties of solids*, 2nd ed. Oxford New York: Oxford University Press, 2010.
- [88] B. Liedberg, C. Nylander, and I. Lunström, "Surface plasmon resonance for gas detection and biosensing," *Sensors and Actuators*, vol. 4, pp. 299-304, // 1983.
- [89] A. G. Brolo, "Plasmonics for future biosensors," *Nat Photon*, vol. 6, pp. 709-713, 2012.
- [90] P. Maraghechi and A. Y. Elezzabi, "Enhanced THz radiation emission from plasmonic complementary Sierpinski fractal emitters," *Optics Express*, vol. 18, pp. 27336-27345.
- [91] L. Rosa, K. Sun, and S. Juodkazis, "Sierpin'ski fractal plasmonic nanoantennas," *physica status solidi (RRL) – Rapid Research Letters*, vol. 5, pp. 175-177.
- [92] L. Guanhai, C. Xiaoshuang, N. Bo, L. Oupeng, H. Lujun, J. Yuan, *et al.*, "Fractal H-shaped plasmonic nanocavity," *Nanotechnology*, vol. 24, p. 205702, 2013.
- [93] F. Miyamaru, Y. Saito, M. W. Takeda, B. Hou, L. Liu, W. Wen, *et al.*, "Terahertz electric response of fractal metamaterial structures," *Physical Review B*, vol. 77, p. 045124, 2008.
- [94] X. Huang, S. Xiao, D. Ye, J. Huangfu, Z. Wang, L. Ran, *et al.*, "Fractal plasmonic metamaterials for subwavelength imaging," *Optics Express*, vol. 18, pp. 10377-10387.
- [95] S. Sederberg and A. Y. Elezzabi, "Sierpinski fractal plasmonic antenna: a fractal abstraction of the plasmonic bowtie antenna," *Optics Express*, vol. 19, pp. 10456-10461.
- [96] B. Hou, X. Q. Liao, and J. K. S. Poon, "Resonant infrared transmission and effective medium response of subwavelength H-fractal apertures," *Optics Express*, vol. 18, pp. 3946-3951.
- [97] S. A. Maier, *Plasmonics: Fundamentals and Applications*. New York Springer, 2007.
- [98] P. G. K. a. M. L. Brongersma, *Surface Plasmon Nanophotonics*, 2007.



- [99] "DiffractMOD User Guide," RSoft Design Group Inc, New York, 2012.
- [100] G. Volpe, G. Volpe, and R. Quidant, "Fractal plasmonics: subdiffraction focusing and broadband spectral response by a Sierpinski nanocarpet," *Optics Express*, vol. 19, pp. 3612-3618.
- [101] P Mühlischlegel, H. J. Eisler, O. J. F. Martin, B. Hecht, and D. W. Pohl, "Resonant Optical Antennas," *Science*, vol. 308, pp. 1607-1609, June 10, 2005 2005.
- [102] D. P. Fromm, A. Sundaramurthy, P. J. Schuck, G. Kino, and W. E. Moerner, "Gap-Dependent Optical Coupling of Single "Bowtie" Nanoantennas Resonant in the Visible," *Nano Letters*, vol. 4, pp. 957-961, 2004.
- [103] H. Fischer and O. J. F. Martin, "Engineering the optical response of plasmonic nanoantennas," *Optics Express*, vol. 16, pp. 9144-9154, 2008.
- [104] S. Kim, J. Jin, Y.-J. Kim, I.-Y. Park, Y. Kim, and S.-W. Kim, "High-harmonic generation by resonant plasmon field enhancement," *Nature*, vol. 453, pp. 757-760, 2008.
- [105] D. K. Cheng, *Fundamentals of engineering electromagnetics*. Reading, Mass.: Addison-Wesley Pub. Co., 1993.
- [106] D. Sarid and W. Challener, *modern introduction to surface plasmons theory mathematica modeling and applications*. Cambridge: Cambridge University Press, 2010.
- [107] L. Eunice Sok Ping, W. Siji, Z. Nan, L. Wei Wei, K. Eng Huat, S. Guang Yuan, *et al.*, "Optical properties of ultrafine line and space polymeric nanogratings coated with metal and metal–dielectric–metal thin films," *Nanotechnology*, vol. 25, p. 055203.
- [108] A. Mooradian, "Photoluminescence of Metals," *Physical Review Letters*, vol. 22, pp. 185-187, 1969.
- [109] G. T. Boyd, Z. H. Yu, and Y. R. Shen, "Photoinduced luminescence from the noble metals and its enhancement on roughened surfaces," *Physical Review B*, vol. 33, pp. 7923-7936, 1986.
- [110] M. Xiao and N. Rakov, "Surface propagation with a large spectral red-shift on a gold thin film containing subwavelength holes," *Physics Letters, Section A: General, Atomic and Solid State Physics*, vol. 309, pp. 452-456, 2003.



- [111] P. L. Stiles, J. A. Dieringer, N. C. Shah, and R. P. Van Duyne, "Surface-enhanced Raman spectroscopy," *Annual Reviews of Analytical Chemistry*, vol. 1, pp. 601-26, 2008.
- [112] B. Sharma, R. R. Frontiera, A.-I. Henry, E. Ringe, and R. P. Van Duyne, "SERS: Materials, applications, and the future," *Materials Today*, vol. 15, pp. 16-25, 2012.
- [113] P. Genevet, J.-P. Tetienne, E. Gatzogiannis, R. Blanchard, M. A. Kats, M. O. Scully, *et al.*, "Large Enhancement of Nonlinear Optical Phenomena by Plasmonic Nanocavity Gratings," *Nano Letters*, vol. 10, pp. 4880-4883, 2010.
- [114] C. K. Chen, T. F. Heinz, D. Ricard, and Y. R. Shen, "Surface-enhanced second-harmonic generation and Raman scattering," *Physical Review B*, vol. 27, pp. 1965-1979, 02/15/ 1983.
- [115] J. C. Hulteen, M. A. Young, and R. P. Van Duyne, "Surface-Enhanced Hyper-Raman Scattering (SEHRS) on Ag Film over Nanosphere (FON) Electrodes: Surface Symmetry of Centrosymmetric Adsorbates," *Langmuir*, vol. 22, pp. 10354-10364, 2006.
- [116] C. B. Milojevich, D. W. Silverstein, L. Jensen, and J. P. Camden, "Probing Two-Photon Properties of Molecules: Large Non-Condon Effects Dominate the Resonance Hyper-Raman Scattering of Rhodamine 6G," *Journal of the American Chemical Society*, vol. 133, pp. 14590-14592, 2011.
- [117] F. Emmanuel and G. Samuel, "Surface enhanced fluorescence," *Journal of Physics D: Applied Physics*, vol. 41, p. 013001, 2008.
- [118] G. M. Koenig, M.V. Meli, J.S. Park, J. J. de Pablo, and N. L. Abbott, "Coupling of the Plasmon Resonances of Chemically Functionalized Gold Nanoparticles to Local Order in Thermotropic Liquid Crystals," *Chemistry of Materials*, vol. 19, pp. 1053-1061, 2007.
- [119] Z. Sun, Y. S. Jung, and H. K. Kim, "Role of surface plasmons in the optical interaction in metallic gratings with narrow slits," *Applied Physics Letters*, vol. 83, pp. 3021-3023, 2003.
- [120] M. Maaza, O. Nemraoui, C. Sella, and A. C. Beye, "Surface Plasmon Resonance Tunability in Au-VO₂ Thermo-chromic Nano-composites," *Gold Bulletin*, vol. 38, pp. 100-106, 2005.



- [121] D. C. Bassett, *Developments in crystalline polymers / edited by D.C. Bassett*. London: Applied Science, 1982.
- [122] F. J. Baltá Calleja, A. G. Arche, T. A. Ezquerro, C. S. Cruz, F. Batallán, B. Frick, *et al.*, "Structure and properties of ferroelectric copolymers of poly(vinylidene fluoride)," in *Structure in Polymers with Special Properties*. vol. 108, H. G. Zachmann, Ed., ed: Springer Berlin Heidelberg, pp. 1-48, 1993.
- [123] A. M. Glass, *Principles and applications of ferroelectrics and related materials*. Oxford [Eng.]: Clarendon Press, 1977.
- [124] S. Ikeda, H. Suzuki, K. Koyama, and Y. Wada, "Second-Order Dielectric Constant of a Copolymer of Vinylidene Fluoride and Trifluoroethylene (52:48 Mole Ratio)," *Polymer Journal*, vol. 19, pp. 681-686, 1987.
- [125] B. Heiler and B. Ploss, "Dielectric nonlinearities of P(VDF-TrFE)," in *Electrets, 1994. (ISE 8), 8th International Symposium, 1994*, pp. 662-667.